Transient optical response and density-evolution of valence electrons in copper after ultrafast laser-excitation

Entwicklung der optischen Eigenschaften und der Valenzelektronendichte in Kupfer nach ultraschneller Laseranregung

Bachelorarbeit in Theoretischer Physik

von

Marius Wenk

durchgeführt am

Fachbereich Physik der TU Kaiserslautern

unter Anleitung von

Prof. Dr. Bärbel Rethfeld

August 2022

Abstract

Ultrashort laser pulses can induce strong modifications of material properties of solids such as creating highly transient optical parameters. After excitation with lasers of high power, the conduction electrons thermalize quickly to a hot Fermi distribution. Yet, the band occupation numbers can still be far from equilibrium.

We study the excitation of copper, based on models introduced for gold with near-infrared (NIR) and visible photons. We use a two-temperature model and construct electron density-resolved rate equations to simulate the non-equilibrium band occupation for two bands, namely the $4sp$- and $3d$-electrons in copper.

Applying the results of the simulation, particularly the occupation and temperature data, we compute the time-resolved dielectric function based on the Drude-Lorentz formalism. In order to compare the results with experimental data, we calculate the transient optical properties such as sample reflectivity and transmissivity. Our predictions are compared with time-resolved measurements of optically excited copper, thus providing insights into electron dynamics on femto- and picosecond timescales.

We investigate the influence of various parameters on the relaxation behavior of copper. Both the parameters used to describe the initial dielectric function and the underlying density of states (DOS) show to have a great effect on transient optical properties. Furthermore, the description of internal energy distribution under the assumption of immediate thermalization of the electrons to Fermi distributions yields reasonable results for the optical response of copper.

Zusammenfassung

Ultrakurze Laserpulse können starke Modifikationen der Materialeigenschaften von Festkörpern bewirken, wie unter anderem sehr kurzzeitige Änderungen der optischen Parameter. Direkt nach der Anregung durch einen Laser mit hoher Leistung thermalisieren die Leitungselektronen zu einer Fermi Verteilung bei erhöhter Temperatur. Dennoch können die Besetzungszahlen der Elektronen deutlich von der Gleichgewichtsverteilung abweichen.

Wir untersuchen die Anregung von Kupfer basierend auf Modellen, die für die Beschreibung von Gold entwickelt und für den nahinfrarot und sichtbaren Bereich des optischen Spektrums konzipiert wurden. Dabei verwenden wir eine Form des Zweitemperaturmodells, bei dem auch die Dichte der Elektronen in den betrachteten Bändern mithilfe von Ratengleichungen bestimmt wird. Damit simulieren wir die Nicht-Gleichgewichtsdynamik basierend auf zwei Elektronenbändern.

Unter Anwendung der Resultate der Simulationen, insbesondere der Bänder und der Temperaturen, berechnen wir, basierend auf dem Drude-Lorentz Formalismus, die zeitabhängige dielektrische Funktion. Um die Ergebnisse mit experimentellen Daten zu vergleichen, berechnen wir zeitabhängige optische Eigenschaften, wie Reflektivität und Transmissivität der Probe. Unsere Vorhersagen werden mit zeitaufgelösten Messungen für optisch angeregtes Kupfer verglichen. Dies liefert Einblicke in die Elektronendynamik auf Zeitskalen im Bereich von Femto- und Pikosekunden.

Wir untersuchen den Einfluss verschiedener Parameter auf das Relaxationsverhalten von Kupfer. Sowohl die Parameter zur Beschreibung der anfänglichen dielektrischen Funktion, als auch die zugrundeliegende Elektronenzustandsdichteverteilung zeigen einen großen Einfluss auf die optischen Eigenschaften während und nach der Bestrahlung. Insgesamt liefert die Beschreibung der internen Energieverteilung unter der Annahme der unmittelbaren Thermalisierung der Elektronen zu einer Fermi Verteilung optische Werte für Kupfer, die gut mit den experimentellen Ergebnissen vergleichbar sind.

Contents

1 Introduction

Energy transitions are essential for modeling the interaction of short-pulse lasers with matter. Understanding the transient processes during equilibration of the probed sample can help to develop new tools for material processing on micrometer scales [1, 2]. Despite strongly spatially localized ablation and heating, high average laser powers can as well lead to extreme conditions, such as those inside planetary cores [3] or stars [4]. Those conditions can indeed only be probed in laboratories in the form of transient states. In order to evaluate the data in such experiments and to optimize surface processing, a thorough understanding of the relaxation processes is of utmost importance. We start with modeling material properties after excitation of thin copper films with near-infrared (NIR) or visible photons, as those are experimentally well tested [5].

The relaxation of laser-excited copper happens on a picosecond timescale [6]. Thus femtosecond laser pulses are a good tool to minimize the interference of the pulse and the relaxation stages. Moreover, optical properties can be probed with femtosecond laser pulses on short timescales, even during phase transitions. This makes them a perfect tool for investigating the material response. Specifically reflectivity and transmissivity can be measured equally well for solids, warm dense matter or plasmas. In the NIR and visible regime, the high laser powers that lead to phase transitions may not be common, but a extension of the model on other initial conditions is possible.

The description of optical photons restricts high energy transitions, as the quantized photon energy is fairly absorbed twice in a row by the same element. This allows for a more precise investigation of the remaining transitions.

The heated copper undergoes several stages of relaxation. After photon-absorption mainly by the electrons, the electrons thermalize fast to a hot Fermi distribution [7]. Yet, the band occupation numbers can still be far from equilibrium. The relaxation between the different electron bands follows. This happens parallel to the electron-phonon relaxation. We approximate the situation by assuming a Fermi distribution to be given at all times. This allows for the use of methods from statistical physics. With the possible microscopic interactions in mind, macroscopic quantities can be modeled to describe the system. Within this approach, the entire energetic distribution of the electrons can be described by determining such statistical parameters for all bands. We use electron band-occupation densities and temperatures as defining macroscopic parameters for these distributions. These parameters can then serve to calculate optical parameters. The presented approach is to determine these internal quantities for the two out-most bands in copper, together with the phonon temperature. This is done

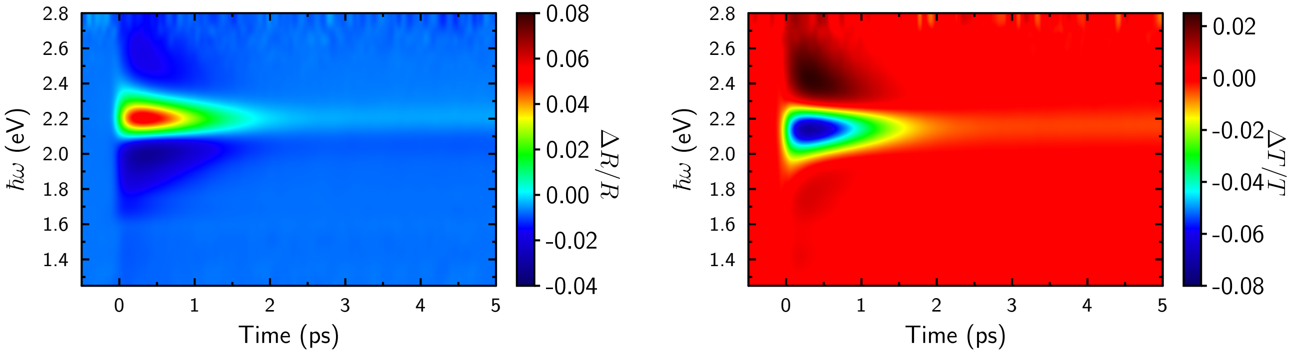

(a) Reflection (b) Transmission

Figure 1.1: Experimental expectations for reflectivity and transmissivity at a thin copper film by Obergfell et al. [5].

by modeling their development with time, starting from a set of initial conditions. In similar models, good agreement with experimental data has been shown for gold [8, 9]. In the approximation of Fermi distributed electrons, the dynamics before electron thermalization can not be described. Still, the energy distribution among the different subsystems on larger timescales seems to be in good agreement with experimental data. We test if this modeling could be generalized for other noble metals, using copper as a starting point with good availability of data.

In a second step, transient optical properties of copper are derived based on a dielectric function that we calculate with a generalized Drude-Lorentz model. We base the time-development of the dielectric function on the evolution of the internal properties, that we described before.

The objective of this thesis is to check, whether the aforementioned assumptions allow for good predictions of transient properties in copper after laser-excitation. Furthermore a time-dependent description of the parameters should be made within reasonable approximations. The aim of the search for such approximations is to simplify calculations. This can allow to make predictions about the laser-matter interaction without the time-expensive use of *abinitio* simulations. Such a model can also serve to understand the underlying statistical processes more intuitively. Moreover, Obergfell et al. [5] present experimental data for reflectivity and transmissivity of thin copper films, excited by a 800 nm laser pulse, probed for several NIR and visible wavelengths. The data is shown in Fig. 1.1. We compare the simulated model-output with these results and present the corresponding internal parameters. As the model ranges beyond such specific pump pulse conditions, we also discuss the influence and evolution of different quantities that are part of the description. We do so based on different sets of pump pulse conditions.

After a short summary of the theoretical foundations for the model (Chapter 2), the two-temperature based two-band rate equation model, developed by the working group [8] will be introduced (Chapter 3) and later discussed for its application on copper (Chapter 4). Following that, the time-variation of transient optical properties within a generalized Drude-Lorentz model will be explained (Chapter 5). Finally, the modeled results will be presented in comparison to the experimental data by Obergfell et al. [5] and discussed (Chapter 6), before giving a conclusion (Chapter 7) and an outlook on possible future investigations and applications regarding the topic (Chapter 8).

2 Solid-State Physics and Laser-Excitation

2.1 Laser-Excitation

In quantum physics, the properties of light can not exclusively be modeled by investigating the fluence or amount of total energy that a laser beam holds. This is, because the energy of the beam is quantized and interactions can basically only happen with energy transfers in portions of these so-called photon energies. The energy E of a photon is connected to the frequency ν of light via

$$E = h\nu, \tag{2.1}$$

where the constant of proportionality h is the Planck constant. A similar expression can be made for the angular frequency $\omega = 2\pi\nu$ as

$$E = \hbar\omega, \tag{2.2}$$

with $\hbar = h/2\pi$. The relation to the wavelength λ

$$\nu = \frac{c}{\lambda}, \tag{2.3}$$

with the speed of light c, yields

$$E = \frac{hc}{\lambda}. \tag{2.4}$$

One main property of the lasers discussed in this work is that they produce highly monochromatic light, such that all photons have the same wavelength.

2.2 Electron Structure in Noble Metals

The electronic structure in solids is defined by the lattice and its quantum mechanical properties. This yields the density of states (DOS) that describes the number of available states at any given electronic energy E. Due to Pauli blocking any state could only be occupied by exactly one fermionic electron. In thermodynamic equilibrium the electron state occupation rate is given by the Fermi distribution f,

$$f(E, \mu, T) = \frac{1}{\exp\left(\frac{E-\mu}{k_B T}\right) + 1}. \tag{2.5}$$

Here, k_B denotes the Boltzmann constant, μ is the chemical potential and T the temperature. The latter is a statistical quantity, that originally only exists in thermal equilibrium. Hence the Fermi distribution applies for the calculation of equilibrium states. As it will be discussed in section 2.3, the Fermi distribution might as well be used vice versa to define the temperature.

The combination of these two distributions along the energy axis gives the full energetic image of the electron distribution in thermal equilibrium. The electron density n of the solid results as

$$n = \int dE \cdot D(E) \cdot f(E, \mu, T_e), \tag{2.6}$$

where D denotes the density of states and T_e the electron temperature.

In a similar fashion, the internal energy density of the electrons is given as

$$u_e = \int dE \cdot E \cdot D(E) \cdot f(E, \mu, T_e). \tag{2.7}$$

The heat capacity for any system, is given via

$$c_j := \frac{du_j}{dT_j}, \tag{2.8}$$

where j is a supplementary index for the respective system. Based on Eq. (2.7), the temperature dependent electron heat capacity can effectively be calculated via

$$c_e(T_e) = \frac{d}{dT_e} \int dE \cdot E \cdot D(E) \cdot f(E, \mu, T_e). \tag{2.9}$$

using the definition in Eq. (2.8).

At temperature $T = 0\,\mathrm{K}$ the Fermi distribution converges to a step function with the step located at the energy of the chemical potential μ, which is also called the Fermi energy E_F. In this situation all states up to the Fermi energy are occupied and all states above this threshold are unoccupied. Together with equation (2.6), the Fermi energy can be determined based on the the electron occupation density n and the DOS.

2.3 Two-Temperature Model

When hit by a femtosecond laser pulse, a metal can absorb the laser energy either via photon-electron or photon-phonon coupling. For light in the visible or NIR range, the photon energies are bigger than the maximum phonon energies and coupling of the lattice with the quantized photons is hence not possible. Furthermore, since the phonon heat capacity is much bigger than that of the electrons, temperature initially rises faster in the electronic system, while the lattice remains relatively cold [10]. This excitation leads to thermodynamic non-equilibrium states [11–13]. Electron-phonon coupling however is possible, as the electron energy can be split continuously. Note, that in this context, lattice, ions and phonons describe the same subsystem. The following thermalization of the electrons to a Fermi distribution happens way faster than the electron-phonon relaxation [5, 7], resulting in a strong non-equilibrium in the energy distribution between phononic and electronic states. For this intermediate timescale, the two-temperature model (TTM) has been put forward [14]. It describes the photonic and electronic energy distributions with two separate temperatures (T_i and T_e) and allows for the use of methods from statistical physics even though thermal equilibrium might not be given. In this sense, the specification of electron temperature instead of a generalized temperature in the Eqs. (2.6) and (2.7) is actually necessary.

2.4 Dielectric function

The optical properties in solids are determined by the time-dependent properties of their charged particles. These are mainly the time-dependent electron properties, when the lattice is considered as the framework for the electronic movement. The dielectric function of the substance describes these properties. For the following optical investigations, the long-wavelength optical limit $\vec{q} \to 0$ applies, as the low frequency photons carry almost no notable impulse. Hence, the dielectric function is exclusively treated under this condition in this description. Note, that the names dielectric function and permittivity are used synonymously. Furthermore, the permittivity is going to be represented in this description by the unit-less relative permittivity ϵ_r

$$\epsilon = \epsilon_r = \frac{\epsilon_a}{\epsilon_0}, \tag{2.10}$$

which is the absolute permittivity ϵ_a, divided by the vacuum permittivity ϵ_0.

For metals, the conduction electrons and the electrons bound to the lattice are considered separately, as they behave differently under the supply of an electric field. The static effect of the electrons bound to the lattice is described with ϵ_b, while the contribution of the quasi-free conduction electrons is given as the optical conductivity σ. These quantities are defined as the following complex constants of proportion [15]

$$\vec{j}(\omega) = \sigma(\omega)\vec{E}(\omega), \tag{2.11}$$

$$\vec{D}(\omega) = \epsilon_b(\omega)\vec{E}(\omega), \tag{2.12}$$

between the electric field vector $\vec{E}$ and the current density $\vec{j}$ or the electric displacement field $\vec{D}$. All of these variables depend on the frequency ω of the light.

With the Maxwell equation for the rotation of the magnetic field in SI-units,

$$\nabla \times \vec{H} = \frac{\partial \vec{D}}{\partial t} + \vec{j} = \epsilon_b \frac{\partial \vec{E}}{\partial t} + \sigma \vec{E} = \left(\epsilon_b + \frac{i\sigma}{\omega}\right) \frac{\partial \vec{E}}{\partial t} = \epsilon \frac{\partial \vec{E}}{\partial t}, \tag{2.13}$$

$$\text{with } \vec{E}(t) = \vec{E}(\omega) e^{-i\omega t}, \tag{2.14}$$

the total complex dielectric function ϵ can be derived as [15]

$$\epsilon(\omega) = \epsilon_b(\omega) + \frac{i\sigma(\omega)}{\omega}. \tag{2.15}$$

The Lorentz formalism for matter wave interaction is designed for dielectric materials. It can be derived, by modeling the forced oscillations of the bound electrons. The light, in its description as an electromagnetic wave, is the source of excitation, for these vibrations. The time-dependent electron properties become frequency-dependent after a Fourier transformation. The resulting oscillation has the frequency of the incoming wave. With classical mechanical calculations for the oscillation and the application of statistics, in order to get to the macroscopic quantity of permittivity, the Lorentz dielectric function can be derived as

$$\epsilon^L(\omega) = \sum_{j=1}^{j_{\max}} \frac{f_j(T_e) \cdot \omega_p^2(T_e)}{\omega_{0,j}^2(T_e) - \omega^2 - i\omega\Gamma_j(T_e)}. \tag{2.16}$$

Here, $\omega_{0,j}$ is the j-th resonance frequency. As the system can have several modes of oscillation, multiple terms for the different resonances are summed up in order to get the total dielectric function. The number of such Lorentz terms is $j_{\max}$. Furthermore, Γ_j describes the damping frequency of the vibration and the oscillator strength f_j is a weighting factor for the different terms of the sum. The oscillator strength is related to the strength of the corresponding absorption mechanism. ω_p is the so-called plasma frequency, that in contrary to the resonance frequencies, is the same for all oscillations in the material and given by

$$\omega_p(T_e) = \sqrt{\frac{n_{\text{free}}(T_e) \cdot e^2}{m_e\epsilon_0}}. \tag{2.17}$$

There, n_{free} is the free-electron density of the material, ϵ_0 is the vacuum permittivity, e the elementary charge and m_e is the electron mass.

The Lorentz dielectric function Eq. (2.16) attributes to the lattice part of the total dielectric function, as it is modeled for bound oscillations. The effect of the free electrons, is described in the Drude dielectric function ϵ^D via

$$\epsilon^D(\omega) = \frac{-f_0\omega_p^2(T_e)}{\omega^2 + i\omega\nu_{\text{total}}(T_i, T_e)}, \tag{2.18}$$

where ν_{total} is the damping frequency for conduction electrons. The damping of free electron oscillations happens due to electron scattering with other electrons or with phonons. Accordingly, it is known as the total electron scattering frequency. f_0 is the free-electron oscillator strength and is given by [16]

$$f_0 = \frac{m_e}{m_e^*}. \tag{2.19}$$

In Eq. (2.19) the quantity m_e^* describes the effective free-electron mass. In pure Drude models, it is often drawn into the plasma frequency like $\omega_p = \sqrt{\frac{n_{\text{free}}(T_e) \cdot e^2}{m_e^*\epsilon_0}}$. This new plasma frequency describes the total coefficient of the Drude term.

Here it becomes apparent, that the Drude dielectric function equals one term of the Lorentz dielectric function, with a resonance frequency of zero and an oscillator strength of f_0. This is explained by the absence of a restoring force for the free electrons in metals. For the bound electrons, this force is induced by the nucleus. Accordingly, both oscillations can be modeled the same way from a mechanical perspective, but with the resonance frequency in the Drude case set to zero.

Both the Lorentz and Drude dielectric function in the formulations of Eq. (2.16) and Eq. (2.18) are fixed to a constant amount of possible oscillations. In the case of the Drude formalism this constant is one. Very often many possible oscillations exist. Some of them may have their resonance frequencies far away from the relevant frequency spectrum. As those terms contribute as a rather constant offset to the values in the observed spectrum, the formulation with an additional fit parameter ϵ_∞, that takes those oscillations into account, is very common. This fit parameter will be introduced in a generalized form in Section 5.1, which is why it is not included in Eq. (2.16) or in Eq. (2.18).

Several quantities are described to be depending on the electron temperature T_e. In band occupation non-equilibrium, the distribution of electrons between the bands also influences these quantities and they become time-dependent, rather than just temperature dependent.

2.4.1 Optical conductivity

As mentioned above, the total scattering frequency consist of a part for electron-electron scattering ν_{ee} and electron-phonon scattering ν_{ei}. As a matter of consistency, the phonons are indicated as ions

$$\nu_{\text{total}}(T_i, T_e) = \nu_{ei}(T_i) + \nu_{ee}(T_e). \tag{2.20}$$

It is also common, to use the scattering rate $\tau = \frac{1}{\nu_{\text{total}}}$ instead of the frequency.

The oscillations of the free electrons under the influence of light define the optical conductivity σ. Therefore, the Drude formalism provides a formula to calculate the complex frequency-dependent electrical conductivity via

$$\sigma(\omega, T_i, T_e) = \frac{\sigma_0(T_i, T_e)}{1 - i\omega\tau(T_i, T_e)}, \tag{2.21}$$

$$\text{with } \sigma_0(T_i, T_e) = \frac{\epsilon_0 \omega_p^2(T_e)}{\nu_{\text{total}}^2(T_i, T_e)}. \tag{2.22}$$

The real part σ_r of Eq. (2.21) is of interest and follows as

$$\sigma_r(\omega, T_i, T_e) = \frac{\sigma_0(T_i, T_e)}{1 + \omega^2\tau^2}. \tag{2.23}$$

σ is often referred to as AC conductivity and σ_0 (Eq. (2.22)) as DC conductivity, because in the limit of small frequencies $\omega \to 0$, the AC conductivity converges towards the DC conductivity.

2.5 Refraction, Absorption, Reflection and Transmission

With the dielectric function at hand, well measurable optical quantities like refractive index, absorption coefficient, reflectivity and transmissivity can be immediately derived from there. The complex index of refraction n is given via

$$n = \sqrt{\epsilon\mu} = n^* + i\kappa, \tag{2.24}$$

where ϵ is the relative permittivity, μ is the relative magnetic permeability, n^* is the real (usual) refractive index and κ is the extinction coefficient. The latter is proportionally connected to the absorption coefficient α, which describes the light-intensity absorption per distance of intrusion into the material

$$\alpha = \frac{2\omega}{c}\kappa. \tag{2.25}$$

Note, that the electron occupation densities and the refractive indices are both conventionally named n, but are not the same. However, the distinction should be possible out of the context. The same is true for the chemical potential and the permeability. Furthermore different notations for the complex and usual refractive index can be found in the literature [15, 17]. As the complex refractive index is most important for our descriptions with a complex dielectric function, it is simply named n here. All the quantities discussed here, are depending on the frequency of the incident light. From a mathematical viewpoint, this derives from the frequency-dependence of the permittivity.

The relative permeabilities μ for usual noble metals are very close to one, such that the complex refractive index in Eq. (2.24) can effectively be described as

$$n = \sqrt{\epsilon}. \tag{2.26}$$

Thus the optical quantities following from this refractive index can be calculated based on the permittivity, as stated initially. The following equations are based on the assumption of $\mu \approx 1$.

The reflection and transmission at free-standing thin films is described by a three-layer system. The system consists of 1. the surrounding material, 2. the film and 3. the surrounding material again. These layers are numbered in order of position relative to the light source. For quantifying the reflection and transmission by thin films, two effects have to be considered. The first effect is the partial reflection of light at each of the two interfaces between surrounding material and film. This effect is caused by differences in the refractive indices. It hence derives from the dielectric functions of both materials. A second effect is the diffraction on thin layers, that is caused by interference of reflected fractions of the incident light, as depicted in Fig. 2.1. This diffraction is

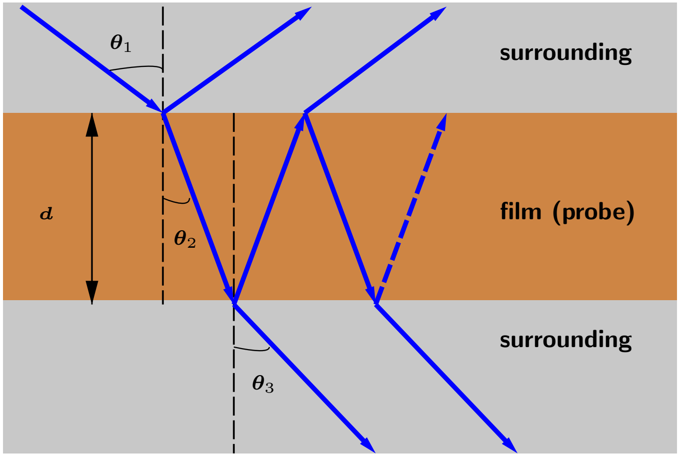

Figure 2.1: Reflection and transmission at thin films.

governed by β, the change in phase, after traveling once from one boundary of the film to the opposite one, following

$$\beta = \frac{2\pi}{\lambda} \cdot d \cdot cos(\theta_2) \cdot n_2. \tag{2.27}$$

Here, d is the thickness of the film, that is only relevant for absorption and diffraction, λ is the probe wavelength, that is the wavelength of the incident light and θ_2 is the angle, that the light has with the surfaces of the film while inside it, see Fig. 2.1. n_2 is the complex refractive index of the film, as in Eq. (2.24), but sub-scripted in order to distinguish it from the one of the surrounding material $n_1 = n_3$. The equations for the characterization of reflection and transmission at thin films are in their most general form described with this complex refractive index. Like this, possible phase shifts and absorptions are included in the formulation without defining any new quantities for their description. Given the phase difference β and the reflection and transmission coefficients r_{12} and t_{12} on entering the film and r_{23} and t_{23} on exiting the film, the total reflection and transmission coefficients r and t of the film can be calculated [17, 18]

$$r = \frac{r_{12} + r_{23}e^{2i\beta}}{1 + r_{12}r_{23}e^{2i\beta}}, \tag{2.28a}$$

$$t = \frac{t_{12}t_{23}e^{i\beta}}{1 + r_{12}r_{23}e^{2i\beta}}. \tag{2.28b}$$

The coefficients for transmission and reflection are connected to the refractive indices of the materials through the Fresnel equations. The strength of the reflection and transmission depends on the polarization of the incident light. Light that is polarized normal or perpendicular to the plane of incidence is called s-polarized, while light that oscillates parallel to the plane of incidence is called p-polarized. Every polarization of light can be evaluated as a combination of those two linear polarizations. The Fresnel equations for the different polarizations are

$$r^s_{(\mathrm{j,j+1})} = \frac{n_j cos(\theta_j) - n_{j+1} cos(\theta_{j+1})}{n_j cos(\theta_j) + n_{j+1} cos(\theta_{j+1})}, \tag{2.29a}$$

$$t^s_{(\mathrm{j,j+1})} = \frac{2 n_j cos(\theta_j)}{n_j cos(\theta_i) + n_{j+1} cos(\theta_{j+1})}, \tag{2.29b}$$

$$r^p_{(\mathrm{j,j+1})} = \frac{n_j cos(\theta_{j+1}) - n_{j+1} cos(\theta_i)}{n_j cos(\theta_{j+1}) + n_{j+1} cos(\theta_j)}, \tag{2.29c}$$

$$t^p_{(\mathrm{j,j+1})} = \frac{2 n_j cos(\theta_j)}{n_j cos(\theta_{j+1}) + n_{j+1} cos(\theta_j)}, \tag{2.29d}$$

with the angle of incidence θ_j and of transmission θ_{j+1} and the refractive indices n_j and n_{j+1} of the two materials in order of position relative to the light source.

Snell's law

$$n_j sin(\theta_j) = n_{j+1} sin(\theta_{j+1}), \tag{2.30}$$

connects the angles of incidence and transmission via the refractive indices of the materials, such that the angle of transmission can be calculated using

$$cos(\theta_{j+1}) = \sqrt{1 - (\frac{n_j}{n_{j+1}} sin(\theta_j))^2}. \tag{2.31}$$

With the formulation in Eq. (2.31), the angle of the light beams inside the film θ_2 can be determined, when the angle of incidence θ_1 is known from experiments. By applying Snell's law twice, the angle after transmission through the entire film θ_3 follows to be equal to the incident angle θ_1. Thus, the total reflection and transmission coefficients of a thin film can be calculated, based on only the polarization of the incident light, the angle of incidence and the refractive indices of all three layers. Therefore, Eq. (2.31) is inserted into the Fresnel equations Eq. (2.29a) and those are used in Eq. (2.28).

For an angle of incidence $\theta_j = 0$, no distinction between s- and p-polarization can be made. This constellation is called normal incidence. The Fresnel equations at normal incidence (subscript n) reduce to the equations

$$r^n_{(\mathrm{j,j+1})} = \frac{n_j - n_{j+1}}{n_j + n_{j+1}}, \tag{2.32a}$$

$$t^n_{(\mathrm{j,j+1})} = \frac{2 n_j}{n_j + n_{j+1}}. \tag{2.32b}$$

Finally, the percentages of reflection and transmission can be expressed as the reflectivity R and transmissivity T via

$$R = |r|^2, \tag{2.33}$$

$$T = \frac{n_3 cos(\theta_3)}{n_1 cos(\theta_1)} |t|^2. \tag{2.34}$$

As the third and first layer are both the same surrounding material, refractive indices and as discussed above angles are equal for both layers. Hence, Eq. (2.34) reduces to $T = |t|^2$, ensuring the real valued-ness of T.

The described method for evaluating reflection and transmission on thin films can be adopted for systems of n layers, where $n \geq 2$ is a natural number, using the so-called matrix method [17].

The portion of the light that is absorbed, the absorption A, results as the remaining part that neither is reflected nor transmitted by the film

$$A = 1 - (R + T), \tag{2.35}$$

such that $A + R + T = 1$.

2.6 Summary

In this chapter, we have presented established theoretical knowledge. Among the parameters that have been introduced are the Fermi distribution and quantities following from this distribution. Also, the dielectric function as well as reflectivity and transmissivity at thin films have been described. With those formulations for optical and statistical properties of solids, the foundation for more specific modeling in the next chapters is given.

3 Two-Band Rate Equation Model for Copper

Our model assumes a Fermi distribution to be given at all times. This is justified, as the excited electrons thermalize to such a quasithermal Fermi distribution faster, than the equilibration between the different electron bands takes [7], even though the thermalization might take up to several hundred femtoseconds [5]. This difference in relaxation time could be explained, as the inter-band particle exchange might take longer, than the intra-band energy exchange. Thus we base our calculations on the two-temperature model (TTM) (see Section 2.3). Kinetic calculations show that the bands share the same temperature shortly after electron thermalization [19, 20]. The modeled electron system is hence at any given time described by the shared electron temperature, the band occupation densities, the chemical potentials and the partial densities of states (pDOS), regarding Eq. (2.6).

During excitation, energy can already be transferred between the electron and phonon system, such that in general both temperatures and heat coefficients change. We consider, that this does not have a significant influence on the absorption of light by phonons and assume all absorbed laser energy to be put into the electronic system, motivated by the analysis in Section 2.3.

The topic of this section is the distribution of energy inside the heated copper with developing time. This distribution is mainly described by statistical parameters like electron band occupation densities and temperatures. There are two purposes of modeling energy distribution inside the copper sample. One is to understand the inner processes in a noble metal after ultrafast laser heating and specifically the relaxation processes on short timescales. The second is to lay the boundaries for calculating further properties, particularly optical ones, that can be evaluated in comparison with experiments. In certain parts of this chapter an outlook on this analysis in Chapter 5 is already given. As in practice there will be not only an excitation with a laser pulse, but also a second probe pulse, we call the exciting laser pulse the pump pulse in order to distinguish between the pulses later. Note, that the physics of excitation with one pulse should work the same, independent of the existence of a following second pulse.

3.1 Band structure in Copper

The electron configuration of copper is [Cu] = [Ar]$3d^{10}4s^1$. The hybridized $4sp$ conduction-band holds one $4s$-electron per ion in the ground state. The remaining free

$4s$ and the $4p$-states are the energetically lowest free states in copper above the Fermi edge. The energetically highest bound electronic states below the Fermi level, are the $3d$-states. We only consider electrons from the two out-most electron orbitals, respectively the $3d$ valence-electrons and the delocalized $4sp$ conduction-electrons. These electrons in total are called the valence electrons. In the following descriptions, the prefix total is meant to describe the totality of these states and electrons, neglecting all the other electrons in copper. This is justified by the application on optical laser-excitation, as the optical photons hardly carry the energy to either excite electrons from deeper states above the minimum band gap of 75.1 eV [21] or to overcome the first ionization energy of 7.73 eV [22]. Here, the minimum band gap of deeper state excitations is the energy difference between the $3p$-states with highest energy and the Fermi edge. Hence, the total electron density for the described states is

$$n = n_{sp} + n_d, \tag{3.1}$$

where n_{sp} is the partial electron density of the $4sp$-electrons and n_d for the $3d$-electrons respectively. As mentioned, this total electron density only changes with the unit cell volume.

Specifically, photon energies ranging from 1.0 to 3.1 eV are investigated in this thesis. These photon energies are indeed smaller than both of the obstacles mentioned above. Accordingly, these obstacles can only be overcome by multiple photons absorption.

The $3d$- and $4sp$- bands are overlapping in the energy range around Fermi energy. In that area, a remarkable part of the electron energy is of kinetic nature. This phenomenon can be understood, given the fact, that these outer electrons have a smaller potential energy than the ones closer to the nucleus, due to Coulomb repulsion, and yet, their total energy is higher. This not only explains, why the electrons above Fermi energy are free and can hence conduct electricity, but it also leads to notable impact interactions of these electrons. Those interactions become important for the optical properties of the excited copper later.

Following, the $3d$- and $4sp$ states will also be referred to, as simply d- and sp-states, as we only discuss those states. Under the assumption of thermalized electrons and now the restriction on two electronic bands, we distinguish between two states of equilibrium. The first such state is the final and real thermal equilibrium at the end of the calculations. The second one is the equilibrium in the electron band occupations. In connection with electrons, we will refer to this simply as equilibrium states. Note, that this equilibrium might exist while electron and phonon temperature may yet be far from equilibrium. Even though we call it equilibrium it would not be a real thermal equilibrium. The equilibrium within one electron band is refered to as electron thermalization to a Fermi distribution.

3.1.1 Electron Density of States

The electronic density of states (DOS) lays the framework for electronic processes in a solid. For the analysis of the band occupation of different electronic subsystems, the partial DOS (pDOS) for each one of them is required respectively.
In this first approach, DOS and pDOS values for solid copper are calculated with density functional theory (DFT), using the FHI-aims Code [23], at a constant temperature of 0 K. In our approximation, the evolution of the DOS with changing electron temperatures is not considered. This is justified, as we do not consider very high laser pulse energies and the DOS calculated with DFT changes very little in a temperature range between 0 up to 10 000 K [24]. However, the model is based on the TTM, such that electron and lattice temperature evolve separately until equilibration.

In consistency with that approximation, the volume of the unit cell of solid copper, is equally presumed to be constant. With changing electron temperatures, the Fermi distribution also changes, while the DOS and total electron density remain constant. Hence, depending on the structure of the DOS, Eq. (2.6) might only be satisfied if the chemical potential changes with the temperature. In order to satisfy this condition, the chemical potential $\mu(T_e)$ can either be defined implicitly by Eq. (2.6), assuming that the $3d$- and $4sp$-bands have the same chemical potential, or in a further distinction, separate chemical potentials for d- and sp-band can be considered. Further on, μ is always going to describe the temperature dependent value, while E_F shall denote the initial and original value of the Fermi energy for solid copper. In the consideration of two distinct chemical potentials, E_F would still be the same for both bands, as it is defined in equilibrium. The partial electron densities n_x^{eq} result as

$$n_x^{eq} = \int dE \cdot D_x(E) \cdot f(E, \mu_x, T_e), \tag{3.2}$$

under the given assumptions and with the above-mentioned notations. Here, D_x is the corresponding pDOS and $x \in \{sp,d\}$. This quantity is defined for Fermi distributed subsystems, regardless of electron-phonon equilibrium. Similar to an implicit definition of a single chemical potential, d- and sp-band chemical potential can be defined based on Eq. (3.2) with $\mu \to \mu_x$.

With Eq. (3.2), a connection between the partial electron densities and the equilibrium chemical potential is given. As this is not a defining equation for the model with one shared chemical potential and both quantities develop formally independently with time, it becomes clear, that the assumption of a shared chemical potential of the $3d$- and $4sp$-bands, is indeed a strong assumption. Thus we consider individual chemical potentials for both bands. Still, in equilibrium, both bands share the same chemical potential, such that a relaxation towards this single chemical potential is indeed expected and introduced into the model. For that reason, the shared or equilibrium chemical potential μ_{eq} is traced with time. This time dependent development would later be discussed again in Chapter 4.

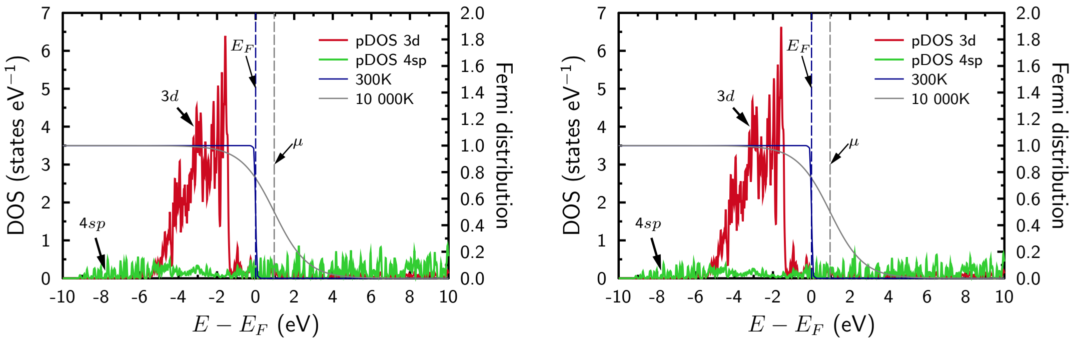

(a) DOS from DFT

(b) Configured DOS from DFT

Figure 3.1: Partial density of states of $3d$- and $4sp$-electrons in copper, determined from DFT-calculations at $T = 0\,\mathrm{K}$, together with equilibrium Fermi distributions at two different temperatures. (a) shows the original calculated values, while in (b) the $3d$-pDOS values are multiplied with $a_d = 1.0372$ and the $4sp$-values are multiplied with $a_{sp} = 0.7573$ in order to calibrate the electron occupation densities with the expected electron numbers (see text and Eq. (3.4)).

Fig. 3.1a shows the mentioned partial DOS and the total DOS, as the sum of the pDOS together with Fermi distributions at 300 K and 10 000 K electron temperature. The Fermi distributions demonstrate the variation of the chemical potential.

In order to calibrate the DOS, the band occupation density numbers are calculated using Eq. (2.6) with $\mu_{eq} = E_F$, $T_e = 300\,\mathrm{K}$ and the partial DOS as input parameters. This temperature is the initial temperature of the simulation. By definition, the extracted values should follow

$$n_x^{eq} = \frac{N_{e,x}}{V}, \tag{3.3}$$

where V is the previously mentioned volume of the unit cell of solid copper and $N_{e,x}$ is the number of electrons (per atom) of the corresponding band in copper. For the two outmost occupied bands in copper, these are $N_{e,4s} = 1$ and $N_{e,3d} = 10$, following from the electron configuration of copper and its hybridization. Note, that there are only one $4s$-electron in equilibrium and no $4p$-electrons. The values calculated with the DOS $n_{\mathrm{DOS},x}$ should equal the values from Eq. (3.3). Hence, a constant a_x is introduced, which is later pulled into the integral in Eq. (2.6) and applied to every value of the corresponding pDOS,

$$n_{\mathrm{DOS},x}^{eq} \cdot a_x = \frac{N_{e,x}}{V} \Rightarrow a_x = \frac{N_{e,x}}{V \cdot n_{\mathrm{DOS},x}^{eq}}. \tag{3.4}$$

With the DFT-DOS, the initial, not-yet calibrated values of the electron density times the unit cell volume are $V \cdot n_{\mathrm{DOS},sp}^{eq} = 1.3205$ for sp-electrons and $V \cdot n_{\mathrm{DOS},d}^{eq} = 9.6412$

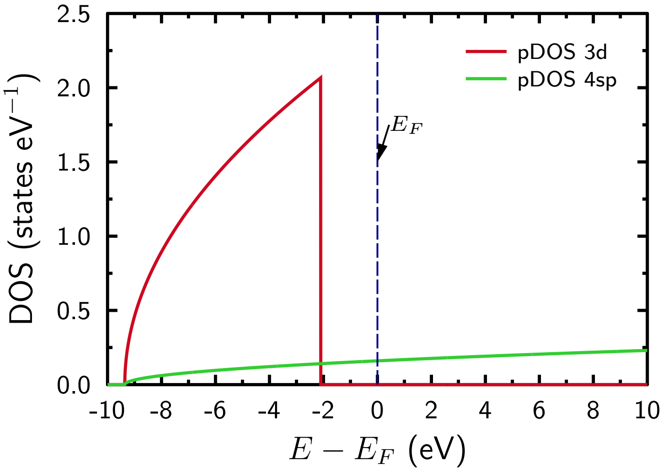

Figure 3.2: Modeled partial density of states of $3d$- and $4sp$-electrons in copper in a parabolic representation.

for d-electrons, thus defining the values $a_{sp} = 0.7573$ and $a_d = 1.0372$. The value used for the unit cell volume of copper at $T = 300\,\mathrm{K}$ is $V = 1.18 \times 10^{-29}\,\mathrm{m}^3$. This is being discussed more specifically in Section 3.3.

Fig. 3.1b shows the modified pDOS and total DOS, in comparison to the original DOS, as in Fig. 3.1a. The difference exists only in stretching and compression of the density values, but the calibrated DOS shall be used for all calculations relying on DFT.

The DFT calculation is not perfect and describes possible $3d$-states above the d-band edge at $2.1\,\mathrm{eV}$ below Fermi energy [5]. In this description Pauli blocking for d-band excitation is weakened, as simulated d-band electrons above the d-band edge can be excited to or above Fermi energy with less energy input. This could lead to major flaws in the description. Hence a very simple alternative model is introduced, to discuss the possible effects of different DOS forms. The pDOS are modeled as parabolic functions with a sharp cut at the band edges and zero at the minimum available energy level in the DFT calculations. For the $4sp$-band, the maximum available energy level of the DFT calculations is taken as band edge. The steepness is set in order to get the correct total electron densities. The resulting curves are presented in Fig. 3.2. The underlying functions are

$$D_x(E) = \begin{cases} b_x\sqrt{E - E_{\min}}, & E \in [E_{\mathrm{min,x}}, E_{\mathrm{max,x}}] \\ 0, & else \end{cases} \tag{3.5}$$

Here, $E_{\mathrm{min,x}}$ and $E_{\mathrm{max,x}}$ are the respective edges of the band, with the hard cut at $E_{\mathrm{max,x}}$. Indeed $E_{min,x} = -9.361\,\mathrm{eV}$ is the same for both bands by construction. The values for

$E_{max,x}$ are $E_{\mathrm{max,sp}} = 43.114\,\mathrm{eV}$ and $E_{\mathrm{max,d}} = -2.1\,\mathrm{eV}$. b_x is a stretching factor, that can be determined through integration, from Eq. (3.3), where b_x can be seen as a constant coefficient to the integral Eq. (3.2). Effectively, this is the same, as for the calibration of the DFT-DOS. The resulting values for b_x are $b_{sp} = 5.238 \times 10^{-2}$ and $b_d = 7.670 \times 10^{-1}$

3.1.2 Electron transitions

Inside the two described electronic bands, yet many different forms of excitation by photons remain possible, but are governed by the described pDOS. For once, intra-band transitions are possible for $4sp$-electrons, mainly independent of the photon energy, as their pDOS is rather flat around the Fermi energy, leading to a similar amount of electrons and free states with the respective energy difference. On the other hand such intra-band transition is little probable for $3d$-electrons, as there are no $3d$-states above the $3d$-band edge and hence Fermi energy. In the DFT-DOS, such states exist but are still few in number. Anyways, they are not an essential property of copper, but rather an error resulting from DFT calculations. Another possible type of transition is inter-band transition. There, an excited electron experiences not only a change of its total energy, but is also transferred into the other electronic band. With the same argument, as for $3d$ intra-band transition, the transition of $4sp$-electrons to $3d$-states hardly occurs. The transition of $3d$-electrons to $4sp$-states is, on the other hand, limited due to the band gap between the high density energies of the $3d$-band and the Fermi energy. This is, because the existing $4sp$-states lying in between are occupied. Consequently, there is a large difference in the frequency of this excitation, depending on whether the photon energy exceeds that gap energy or not.

Another possibility is that of multiple photons absorption, where one electron absorbs several photons and thus several photon energies consecutively. This signifies, that the intermittent states with lower numbers of photon-energy differences to the initial state of the electron are of no relevance to this transition. Thus Pauli blocking of those states is of no importance. Yet, Pauli blocking exists for the states of the final electron energy. The probability of such transitions depends on the electron-photon coupling dynamics connected to the initial and final electron states. This process results to be really improbable even for two photon absorption. In approximation, we hence do not consider this effect in the rate equation system. Accordingly, in our model, every absorbed photon energy leads to the excitation of exactly one electron.

The aforementioned analysis, is done for the initial electron distribution in copper at 300 K. Here, the absorbed energy density comes to importance. If the absorbed energy density is low, and especially the absorbed energy density per photon energy is low, then only a few changes from the initial occupation state occur. In this case, the very same analysis could be applied for the entire time evolution. If on the other hand, the absorbed energy density is high, the occupation changes heavily during the laser-excitation, and states that were blocked initially can become free, enabling the transition into them. This, however, can in approximation be neglected for the absorbed energy densities, that are going to be analyzed in this work. Yet, the description of these processes on smaller timescales, at which electron distributions do not follow a Fermi distribution, is possible for instance with Boltzmann collision integrals [25].

Consequently, considering the $3d$ to $4sp$ transitions as inter-band transitions and the $4sp$ to $4sp$ transitions as intra-band transitions, the absorption rate for each of the two bands shall be quantified, with an absorption coefficient (α_{inter} and α_{intra} respectively),

$$\alpha_{\text{inter}} = \alpha_{\text{total}} \frac{\Omega_d}{\Omega_d + \Omega_{sp}}, \tag{3.6a}$$

$$\alpha_{\text{intra}} = \alpha_{\text{total}} \frac{\Omega_{sp}}{\Omega_d + \Omega_{sp}}. \tag{3.6b}$$

$$\tag{3.6c}$$

Here, Ω_d and Ω_{sp} are the numbers of electrons respectively in the $3d$- and $4sp$-band, that can absorb photons with the given photon energy of $\hbar\omega_{\text{pump}}$ and hence be excited into the $4sp$-band. The fractions give the percentage of excitable electrons in the respective bands, as all possible excitations are assumed to be equally probable. Both terms are governed by the total absorption coefficient α_{total}. As by construction, the two partial absorption coefficients sum up to the total absorption coefficient [Eq. (3.7)]

$$\alpha_{\text{total}} = \alpha_{\text{inter}} + \alpha_{\text{intra}}. \tag{3.7}$$

The numbers of absorbing electrons are calculated via

$$\Omega_x = \int dE \cdot D_x(E) \cdot f(E, \mu_x, T_e) \cdot [1 - f(E + \hbar\omega_{\text{pump}}, \mu_{sp}, T_e)], \tag{3.8}$$

and thus determined by the number of available electrons and the percentage of unoccupied $4sp$-target states at the target energy of $E + \hbar\omega_{\text{pump}}$. The latter is implemented through the Pauli blocking factor [1 - f].

The portion of photons absorbed by d-band electrons is presented in Fig. 3.3 for two different models for the pDOS. It strongly depends on the energy of the absorbed photons for energies around and below the $3d$-band edge. Here the form of the DOS has a huge effect as well. This can be explained, as photons below the d-band edge can not excite d-electrons above the Fermi edge and hence to the majority of free states. With a less defined d-band, this effect of Pauli blocking becomes weaker. For high photon energies, the ratio is more or less constant, as Pauli blocking has no huge effect anymore. The value for such energies lies around 95 %. Hence, as soon as it becomes possible, the absorption of d-electrons is indeed dominating the process.

3.2 Rate Equation System

The model describes processes after laser-excitation with photon energies, such that laser induced electronic band transition only takes place between the $4sp$- and the $3d$-

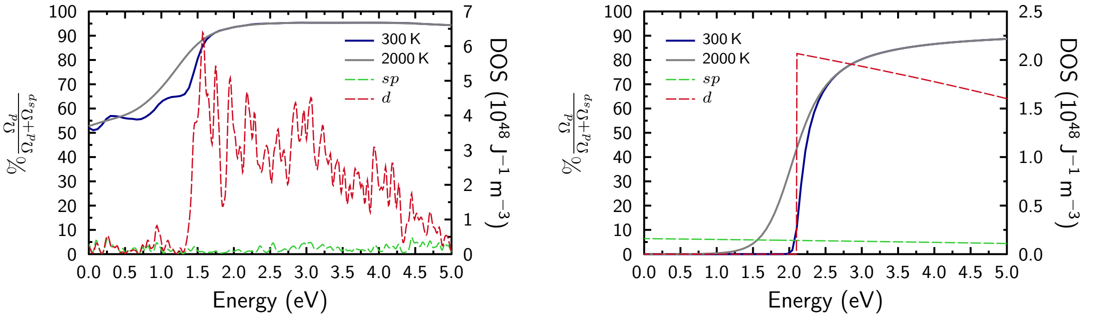

(a) DFT-DOS (b) parabolic-DOS

Figure 3.3: Percentage of inter-band absorption for (a) the DFT-DOS and (b) the parabolic-DOS.

band. Following the excitation, the electrons relax back to their equilibrium occupation densities. The model includes the energy transfer from the electrons to the lattice as a transition of temperature between both systems. These dynamics are modeled with a system of rate equations, as

$$\frac{dn_{sp}}{dt} = \alpha_{\text{inter}} \frac{i_L(t)}{\hbar\omega_{\text{pump}}} - \frac{1}{\tau_{\text{relax}}}(n_{sp} - n_{sp}^{eq}(T_e)) = -\frac{dn_d}{dt}, \tag{3.9a}$$

$$c_e(T_e)\frac{dT_e}{dt} = \frac{du_e}{dt} = \alpha_{\text{total}} i_L(t) - g_{ei}(T_e)(T_e - T_i), \tag{3.9b}$$

$$c_i\frac{dT_i}{dt} = \frac{du_i}{dt} = g_{ei}(T_e)(T_e - T_i), \tag{3.9c}$$

where the Eqs. (3.9b) and (3.9c) hold valid, because of Eq. (2.8).

Note, that all small thermodynamical variables are meant to represent their value per volume throughout this work. The variables are described this way, because it generalizes the model to be independent of the sample volume and represents the situation, that the laser heats with a certain energy density per volume or at least per surface.

Eq. (3.9a) traces the time evolution of the $4sp$-conduction band, as well as the $3d$-band, while Eq. (3.9b) and Eq. (3.9c) describe the time evolution of the temperature of the two upper electron bands and the lattice, respectively.

The time-development of the band occupation in the $4sp$-band is opposed to the one for the $3d$-band, as electrons are exclusively transferred between them, which leads to the second equality in Eq. (3.9a).

The center of Eq. (3.9a) consists of two terms. The first one describes the increase of the population in the $4sp$-band and respectively the decrease in the $3d$-band, due to photo excitation of $3d$-electrons to the $4sp$-band by the laser. This happens in proportion to the laser intensity $i_L(t)$ that describes the absorbed laser energy per time and volume. In order to extract the number of excited electrons per time and volume this source term is divided by the energy of one photon $\hbar\omega_{\text{pump}}$. Here, only single photon absorption is considered, as described in Section 3.1.2. In order to distinguish the inter-band from the intra-band transitions, where the latter transitions are not contributing to population changes, this electron excitation term is multiplied by the inter-band absorption coefficient α_{inter} [Eq. (3.6a)], that as well takes into account possible reflections or transmissions of photons.

The second term in Eq. (3.9a) describes the equilibration of the occupation densities. Here, impact ionization and electron-hole recombination processes, are driving this relaxation, as they are balanced only in equilibrium. The term describes an exponential decay of n_{sp} to the equilibrium density $n_{sp}^{eq}(T_e)$, with a inter-band relaxation time τ_{relax}, also called electron internal thermalization time. The equilibrium density is defined by Eq. (3.2) as well, but with the equilibrium chemical potential μ_{eq} instead of μ_{sp}. Consequently, the equilibration of occupation densities is better described as the equilibration of chemical potentials. Note, that the transient equilibrium states for the chemical potential change with the electron temperature and thus with time, as the electrons equilibrate with the phonons. Therefore, the final equilibration time is not solely described by the inter-band relaxation time, even after the laser-excitation has stopped.

The first equalities in the Eqs. (3.9b) and (3.9c) represent the fact, that the model actually describes the evolution of the internal energy of the electronic and phononic system respectively. For the determination of for example the Fermi distribution, the corresponding temperature is required. Therefore the time-developments of the internal energies are transformed to determine the temperature developments, using the respective heat capacities per volume $c_e(T_e)$ and c_i, as defined by Eq. (2.8). The electron heat capacity is temperature dependent and is defined via Eq. (2.9).

The first term on the left side of Eq. (3.9b) accounts for the change of internal energy due to laser heating. It consists of the laser intensity $i_L(t)$ times the total absorption coefficient α_{total}.

The second term on the left side of Eq. (3.9b) and the left side of Eq. (3.9c) trace the energy transfer between the electron and phonon system. This is proportional to the temperature difference, such that in thermal equilibrium no further energy is transferred. It is determined by the electron-phonon coupling coefficient $g_{ei}(T_e)$. The temperature exchange with the surroundings is not of interest for understanding the processes inside the sample on such timescales and can also be neglected for experiments performed in vacuum. It is hence not listed here.

In summary, the model assumes a time-independent DOS-occupation, a shared electron temperature and restricted possibilities for electron and photon transitions and couplings. Additionally, all calculations are at all times based on Fermi-distributed electrons. The following calculations are based on those assumptions.

3.2.1 Calculation of the Evolution of Electron Temperature and Chemical Potential

Within the model, the explicit determination of the electron heat capacity is not necessary and thus not part of this work, but formulae exist for laser-excited copper [26]. We expand several first time-derivatives analytically in order to calculate the one of the electron temperature, based on Eq. (3.9b). All of the statistical quantities are modeled to exist for both *sp*- and *d*-band. Therefore calculations can be performed for both bands separately. Furthermore, a third system, for the equilibrium distribution between both bands can also be traced with time independently. For the chemical potential, three different values describe these three systems and can be calculated in connection with the respective system. The electron temperature is assumed to be the same for all of the three systems. We trace the electron temperature for the equilibrium system. Even though equilibrium might not exist at all times, its time-development can still formally be calculated equally well. Furthermore, a direct connection to either single band is avoided.

Internal energy and electron density of the various electron systems depend on the electron temperature and the corresponding chemical potential, as follows from Eq. (2.7) and Eq. (2.6). Thus, with $u_{e,x} = u_{e,x}(T_e, \mu_x)$ and $n_x = n_x(T_e, \mu_x)$, their first derivatives can be determined via

$$\frac{du_{e,x}}{dt} = \frac{\partial u_{e,x}}{\partial T_e}\frac{dT_e}{dt} + \frac{\partial u_{e,x}}{\partial \mu_x}\frac{d\mu_x}{dt}, \tag{3.10a}$$

$$\frac{dn_x}{dt} = \frac{\partial n_x}{\partial T_e}\frac{dT_e}{dt} + \frac{\partial n_x}{\partial \mu_x}\frac{d\mu_x}{dt}, \tag{3.10b}$$

where now $x \in [sp, d, eq]$ covers the equilibrium state as well, connected to the total internal electron energy u_e and electron density n.

Now all of the partial derivatives in Eqs. (3.10) can be calculated explicitly, using Eqs. (2.6) and (2.7)

$$c^x_{T_e} := \frac{\partial u_{e,x}}{\partial T_e} = \frac{\partial}{\partial T_e}\int dE \cdot E \cdot D_x(E) \cdot f(E, \mu_x, T_e), \tag{3.11a}$$

$$c^x_{\mu} := \frac{\partial u_{e,x}}{\partial \mu_x} = \frac{\partial}{\partial \mu_x}\int dE \cdot E \cdot D_x(E) \cdot f(E, \mu, T_e), \tag{3.11b}$$

$$p^x_{T_e} := \frac{\partial n_x}{\partial T_e} = \frac{\partial}{\partial T_e}\int dE \cdot D_x(E) \cdot f(E, \mu_x, T_e), \tag{3.11c}$$

$$p^x_{\mu} := \frac{\partial n_x}{\partial \mu_x} = \frac{\partial}{\partial \mu_x}\int dE \cdot D_x(E) \cdot f(E, \mu_x, T_e). \tag{3.11d}$$

With these abbreviations, Eqs. (3.10) can be dissolved to the quantities $\frac{dT_e}{dt}$ and $\frac{d\mu}{dt}$ that we aim to calculate,

$$\frac{dT_e}{dt} = \frac{1}{c^x_{T_e}} \left[\frac{du_{e,x}}{dt} - c^x_\mu \frac{d\mu_x}{dt}\right], \tag{3.12}$$

$$\frac{d\mu_x}{dt} = \frac{1}{p^x_\mu} \left[\frac{dn_x}{dt} - p^x_{T_e} \frac{dT_e}{dt}\right], \tag{3.13}$$

given that $c^x_{T_e}$ and p^x_μ have non-zero values. The temperature development follows from the equilibrium case via

$$\begin{aligned} \frac{dT_e}{dt} &= \frac{1}{c^{eq}_{T_e}} \left[\frac{du_e}{dt} - c^{eq}_\mu \frac{1}{p^{eq}_\mu}\left(\frac{dn}{dt} - p_{T_e}\frac{dT_e}{dt}\right)\right] \\ &= \frac{1}{c_{T_e}}\frac{du_e}{dt} - \frac{c^{eq}_\mu}{c^{eq}_{T_e}}\frac{1}{p^{eq}_\mu}\frac{dn}{dt} + \frac{c^{eq}_\mu}{c^{eq}_{T_e}}\frac{p^{eq}_{T_e}}{p^{eq}_\mu}\frac{dT_e}{dt} \\ \Rightarrow \frac{dT_e}{dt}\left(1 - \frac{c^{eq}_\mu}{c^{eq}_{T_e}}\frac{p^{eq}_{T_e}}{p^{eq}_\mu}\right) &= \frac{1}{c^{eq}_{T_e}}\left(\frac{du_e}{dt} - \frac{c^{eq}_\mu}{p^{eq}_\mu}\frac{dn}{dt}\right) \\ \Rightarrow \frac{dT_e}{dt} &= \frac{\frac{1}{c^{eq}_{T_e}}\left(\frac{du_e}{dt} - \frac{c^{eq}_\mu}{p^{eq}_\mu}\frac{dn}{dt}\right)}{\left(1 - \frac{c^{eq}_\mu}{c^{eq}_{T_e}}\frac{p^{eq}_{T_e}}{p^{eq}_\mu}\right)}. \end{aligned} \tag{3.14}$$

Given this equation, the calculation of the chemical potentials is completely given by Eq. (3.13).

The partial derivatives described in Eqs. (3.11) reduce to integrals over the derived Fermi distributions. These are

$$\frac{\partial f}{\partial T} = \frac{E-\mu}{k_B T^2} \cdot \frac{\exp\left(\frac{E-\mu}{k_BT}\right)}{\left(\exp\left(\frac{E-\mu}{k_BT}\right)+1\right)^2} = \frac{E-\mu}{k_B T^2} \cdot \frac{1}{2 + 2cosh\left(\frac{E-\mu}{k_BT}\right)}, \tag{3.15}$$

$$\frac{\partial f}{\partial \mu} = \frac{1}{k_B T} \cdot \frac{\exp\left(\frac{E-\mu}{k_BT}\right)}{\left(\exp\left(\frac{E-\mu}{k_BT}\right)+1\right)^2} = \frac{1}{k_B T} \cdot \frac{1}{2 + 2cosh\left(\frac{E-\mu}{k_BT}\right)}. \tag{3.16}$$

3.2.2 Laser Heating

In order to model the laser heating of the system, an ideal Gaussian pulse with pulse duration τ_p is used as laser intensity distribution. The pulse duration is the FWHM (full width at half maximum) of the Gaussian distribution. This is expressed as

$$i_L(t) = \sqrt{\frac{4ln(2)}{\pi}}\frac{u^{em}_L}{\tau_p} \exp\left[-4ln(2)\left(\frac{t^2}{\tau_p^2}\right)\right], \tag{3.17}$$

where u^{em}_L is the total emitted laser energy per surface. Mathematically, u^{em}_L equals the surface under the Gaussian function or the value of the integral over $i_L(t)$. In experiments this pulse form is indeed also being used, but with possible external disturbances. Furthermore this pulse form is comparably easy to create on femtosecond timescales.

The laser intensity is for the purposes of this model solely used in combination with the total absorption coefficient or a fraction of it, in order to determine the laser energy absorbed by the copper sample. This supports the use of the laser source term $s_L = \alpha i_L$, where instead of the emitted laser energy per surface, the absorbed laser energy per volume u_L^{ab} is used, with

$$u_L^{ab} = \alpha u_L^{em}. \tag{3.18}$$

The conversion from surface to volume is included by the absorption, which has the unit m^{-1}. Often, the absorbed energy per mass $\Delta\epsilon$ can be measured experimentally and the absorbed energy per volume determined via

$$u_L^{ab} = \rho\Delta\epsilon, \tag{3.19}$$

where ρ is the mass density of copper.

This approach assumes constant values of absorption, even though the electronic occupations may already change during laser-excitation and therefore alter the absorption. However, these effects are considered to be small and the temperature dependent non-equilibrium absorption could only be calculated when the exact material properties are known. Those properties are on the other hand calculated based on the laser heating, so a calculation would end up into a loop and is thus not possible without further assumptions.

3.3 Applied Material Parameters

The electron-phonon coupling parameter is taken from Ref. [26] of Lin et al., where it is calculated within the boundaries of the TTM. However, other approaches incorporating molecular-dynamics (MD) simulations exist [27, 28]. It is known, that nonthermalized electron systems couple differently to the lattice than the thermalized ones [29, 30]. Thus the use of the Lin formula for thermalized electrons is the most consistent one, with the assumption of thermalized electrons at all times.

For the density of copper we use the mass density $\rho = 8.94\,\mathrm{g\,cm^{-3}}$ at room temperature [31], as the mass density is determined by the lattice and the lattice is not expected to change significantly in temperature during the laser-excitation, for which the mass density is considered. This approach is as well consistent with the assumption of constant unit cell volume throughout the experiment, that was already proposed in connection with the time-independent DOS-occupation. The basis for all those assumptions, is the idea, that the heated material needs time to expand and thus remains constant in volume on very short timescales. This would as well lead to said extreme conditions, where the density is relatively high compared to the temperature. The constant unit cell volume is extracted from the density, as the volume of the mass of one copper atom $m_{Cu} = 63.55\,\mathrm{u}$. The unit cell volume follows as $V = 1.18 \times 10^{-29}\,\mathrm{m}^3$.

As opposed to the electron heat capacity, the phonon heat capacity is assumed to be constant. For sufficiently high temperatures, that are given for the laser heating starting from 300 K, the Dulong-Petit law is applied in good approximation, as done in other calculations for ultrafast laser-excitation considering the TTM [13, 26]. The molar phonon heat capacity hence is considered to be $24.9\,\mathrm{J\,mol^{-1}\,K^{-1}}$. Divided by the molar mass of $63.55\,\mathrm{g\,mol^{-1}}$ and multiplied with the density ρ, the phonon heat capacity per volume results as $c_i = 3.503\,\mathrm{MJ\,m^{-3}\,K^{-1}}$ in good agreement with $c_i = 3.449\,\mathrm{MJ\,m^{-3}\,K^{-1}}$ as used in Ref. [7].

The electron internal thermalization time τ_{relax} of copper is not as well established, as other material properties. Thus, we leave it as a free fitting parameter at first, in order to discuss its influence on the temporal development of the electron densities. However, for further calculations, we consider the value extracted by Shen et al. $\tau_{\mathrm{relax}} = 258\,\mathrm{fs}$ [7] again without the error 31 fs. Also, the electron-phonon relaxation time is presented as $\tau_{ei} = 510\,\mathrm{fs}$ [7], that is more or less two times the inter-band relaxation time. It can hence be expected, that the electrons equilibrate faster, than the electron-phonon interaction takes place. This supports initial assumptions and beyond that gives reason to expect, that the secondary phonon heating during the fast laser-excitation is indeed rather small.

The remaining properties are properties of the pump pulse, that shall be varied within the range the model is made for, for further understanding in Chapter 4.

3.4 Numerics

The rate equation system Eq. (3.9) is complemented with calculations of underlying parameters in Section 3.2.1 and yields a complete system of ordinary differential equations (ODE). The parameters expressed and traced by their time derivatives are n_{sp}, n_d, $n = n_{sp} + n_d$, u_e, T_e, T_i, μ_{sp}, μ_d and μ_{eq}. The ODE is solved with Dormand-Prince (DOPRI) numerical integration. The method is a type of Runge-Kutta integration of order five.

For solving the ODE system, every time step is calculated from the values of the time before, such that only the initial conditions and the development with time have to be known. We use time steps of 0.1 fs and a total range of times between $-1\,\mathrm{ps}$ and 10 ps for our calculations.

3.5 Summary

In this chapter, we have presented specific descriptions for solids, that we use to model laser-excited copper. The main focus has been on the distribution of electrons in copper. Therefore, we have introduced and configured several pDOS descriptions, in order to make them agree with other statistical quantities. We have also discussed the possible electron transitions in the observed situation. Furthermore, we have described the assumptions, that lay the foundation of our model and aim to simplify the calculations without loosing too much accuracy. Such assumptions have been the limitation of possible laser-excited electron transitions on those from the $3d$- or $4sp$-band into the $4sp$-band and the assumption of Fermi distributed electrons at all times. Additionally, we have assumed a shared temperature for both electron bands. Yet, the description has been made within the TTM, with a separate ion temperature for the lattice.

In Section 3.2, the core of the two-band electron density model has been introduced with the analytical description of the evolution of temperature, electron density, chemical potential and internal energy. Following that, the relevant parameters for copper and the numerical method of Runge-Kutta integration for solving these equations have been discussed.

In the next chapter, we will present the resulting values over time and discuss the implications of our model.

4 Transient Electron Density and Temperature in Copper

The time-development of the various material properties modeled by Eqs. (3.9), result to be strongly dependent of the properties on the laser pump pulse. Even though connections between different material properties exist, some of them still remain independent of many other parameters in the model. This behavior can be immediately extracted from Eqs. (3.9). For example the temperature development is completely independent of the electron internal thermalization time τ_{relax}. Similarly, the laser frequency ω_{pump} influences the inter- and intra-band heating relation, as well as consequently the *d*- and *sp*-electron density, but for the temperature increase, only the total amount of absorbed energy and not its quantization is of importance. It should be mentioned, however, that strong variations in the photon energy can perhaps change the mode of interaction completely, such that the material might for example be ablated. The model after all makes assumptions and is designed in certain boundaries.

We present the data for two sets of laser pulse conditions. Around those conditions, isolated variations of parameters are made, in order to compare their influence.

The first set of parameters has the pump pulse data of Obergfell et al. [5] and such presents the conditions for experimental comparison. It is presented in Table 4.1 as Set (a). With these parameters, the pump energy density and the photon energies are rather low, compared to the range of energies, the model is designed for. Thus, a second set of parameters is introduced in Table 4.1(b) for making a better discussion of the model possible. The photon energy of $\hbar\omega_{\mathrm{pump}} = 1.55\,\mathrm{eV}$ in Table 4.1(a) is below the theoretical *d*-band edge of 2.1 eV and hence yields small interaction between *d*- and *sp*-band. Furthermore, the electron thermalization time for various noble metals is expected to be smaller for higher absorbed energies [29]. The investigation at a higher absorbed laser energy hence justifies the assumption of immediate electron thermalization better. In Table 4.1, the values for laser wavelength and photon energy are connected via Eq. (2.4), but are both relevant for a intuitive discussion. The laser intensity peak is set to lie at $t = 0\,\mathrm{fs}$, as implemented in Eq. (3.17). The electron-electron relaxation time τ_{relax} is taken from Section 3.3.

Table 4.1: Two sets of pump pulse parameters of the laser, used for simulations of transient properties in copper.

Set	(a)	(b)
τ_p (FWHM)	50 fs	50 fs
τ_{relax}	258 fs	258 fs
u_L^{ab}	$54\,\mathrm{J\,cm^{-3}}$	$5400\,\mathrm{J\,cm^{-3}}$
λ_{pump}	800 nm	400 nm
$\hbar\omega_{\text{pump}}$	1.55 eV	3.1 eV

4.1 Electron distribution

4.1.1 Comparison of Two Sets of Laser Conditions

The *sp*-densities are presented in Fig. 4.1 for the DFT-DOS. In direct comparison, the high energy pulse with parameters from Table 4.1(b), yields a far stronger increase in the 4*sp*-density, as the number of photons is bigger. The number of photons is proportional to the absorbed energy and the inverse of the photon energy, but the increase in absorbed energy dominates the doubled photon energy for the data of Table 4.1(b). Additionally, the relative interband absorption ratio is bigger for the photon energy of 3.1 eV with parameters from Table 4.1(b), as presented in Fig. 3.3a, where the initial absorption ratio is 84.52 % for the parameters from Table 4.1(a) and 95.32 % for the parameters from Table 4.1(b). The effect of the different interband

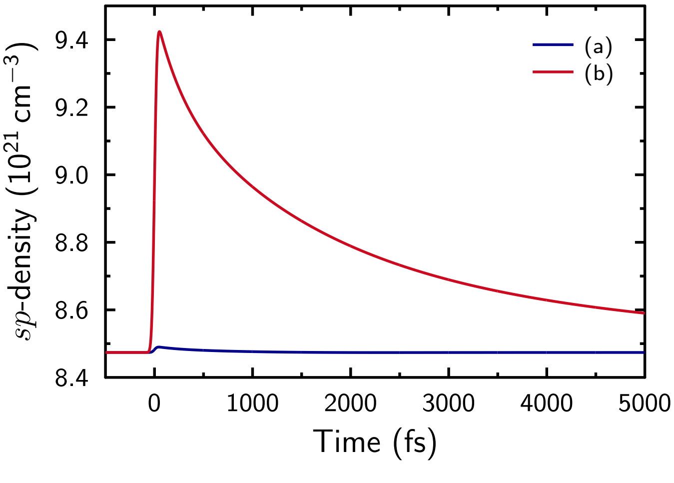

Figure 4.1: Simulated *sp*-band densities n_{sp}, for pump pulse parameters from Table 4.1(a) and Table 4.1(b), based on the DFT-DOS.

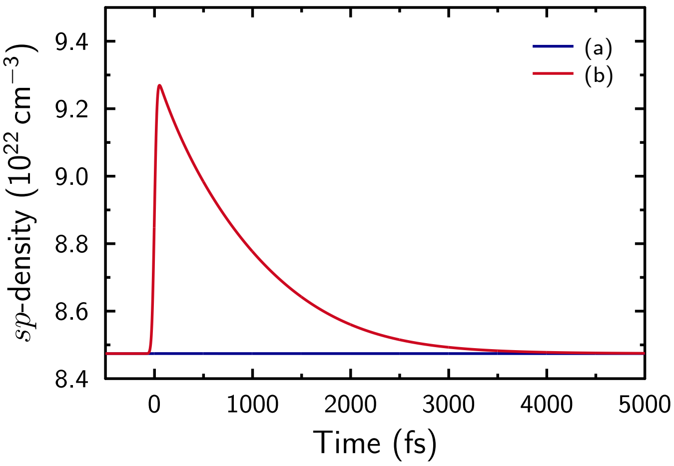

Figure 4.2: Simulated sp-band densities n_{sp}, for pump pulse parameters from Table 4.1(a) and Table 4.1(b), based on the parabolic-DOS.

absorptions becomes more apparent, with the use of the parabolic-DOS, in Fig. 4.2, where the initial absorption ratio is $1.17 \times 10^{-8}\,\%$ for the parameters from Table 4.1(a) and $81.45\,\%$ for the parameters from Table 4.1(b). Accordingly, the only change in n_{sp} for the parabolic-DOS excited with $\lambda_{\text{pump}} = 800\,\text{nm}$ is a small increase towards the new band occupation equilibrium at high times.

Figs. 4.3 show the time-development of the sp-densities for different relaxation

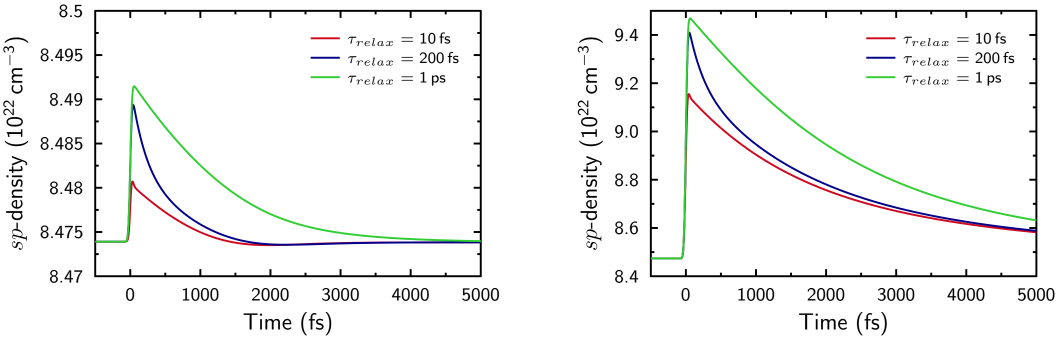

(a) Parameters from Table 4.1(a)

(b) Parameters from Table 4.1(b)

Figure 4.3: Simulated sp-band densities n_{sp}, for different electron-electron relaxation times τ_{relax}, based on the DFT-DOS, for pump pulse parameters from Table 4.1(a) in (a) and from Table 4.1(b) in (b) (except for τ_{relax}).

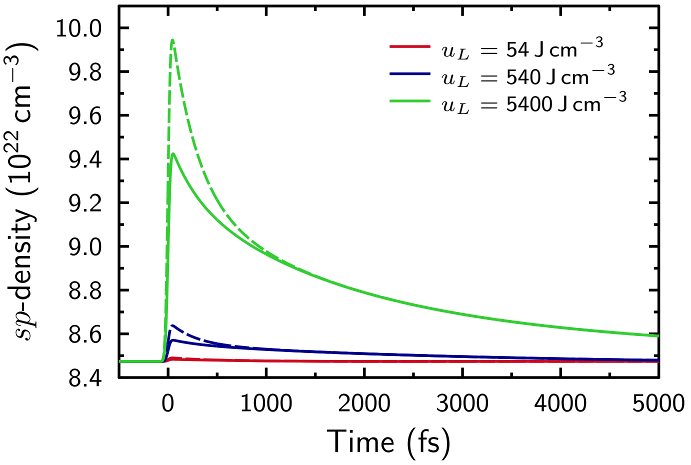

Figure 4.4: Simulated sp-band densities n_{sp} for different total absorbed laser energies u_L, based on the DFT-DOS, for an electron-electron relaxation time of $\tau_{\text{relax}} = 258\,\text{fs}$ and pump pulse wavelengths of $\lambda_{\text{pump}} = 400\,\text{nm}$ (solid lines) and $\lambda_{\text{pump}} = 800\,\text{nm}$ (dashed lines). Accordingly, the dashed red line corresponds to Table 4.1(a) and the solid green line to Table 4.1(b).

times. Clearly, the relaxation times have an important impact on the relaxation behavior. For faster relaxation times, a relaxation seems to take place even during laser-excitation, such that the maximum sp-density does not reach as high values, as for higher relaxation times. The effect is the most significant for $\tau_{\text{relax}} = 10\,\text{fs}$, which is indeed smaller, than the pump pulse duration of $\tau_p = 50\,\text{fs}$. The following relaxation behavior also differs greatly. At the lower excitation energies in Fig. 4.3a, the sp-densities for $\tau_{\text{relax}} = 10\,\text{fs}$ and $\tau_{\text{relax}} = 200\,\text{fs}$ can be seen to drop below their initial values, with minima at $t = 1982\,\text{fs}$ and $t = 2239\,\text{fs}$ respectively. This effect of overshooting electron densities points out the limitations on accuracy of the numerics, as such an overshoot should not take place considering the underlying equations. For very low laser energies, the total values are small enough so that consecutive errors in the finite numerical calculations lead to notable effects. Similar or more important errors occur for calculating with very low photon energies, as the model is not designed for such energies. Apparently the model reaches its limits around a photon energy of $\hbar\omega_{\text{pump}} = 1\,\text{eV}$.

4.1.2 Systematic Modulation of the Absorbed Laser Energy

In comparison, the maximum in sp-density clearly increases with the absorbed laser energy, as more photons are available for initializing the interband transition, as presented in Fig. 4.4, for the DFT-DOS. The DFT-DOS yields high enough interband absorption ratios for both 400 nm and 800 nm pulses, that a recognizable increase takes place even

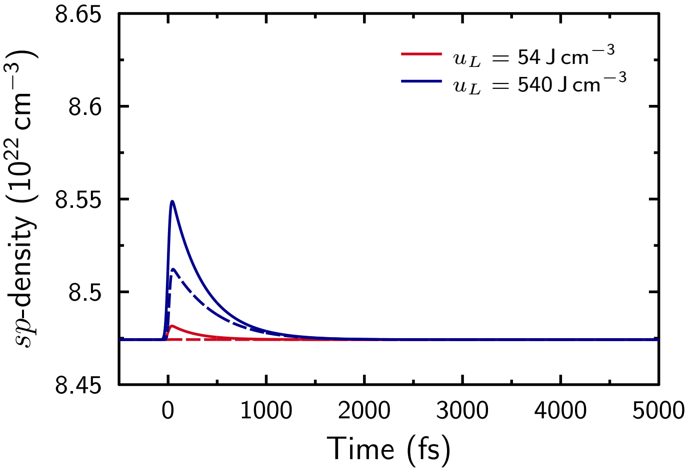

Figure 4.5: Simulated sp-band densities n_{sp} for different total absorbed laser energies u_L, based on the parabolic-DOS, for an electron-electron relaxation time of $\tau_{\text{relax}} = 258\,\text{fs}$ and pump pulse wavelengths of $\lambda_{\text{pump}} = 400\,\text{nm}$ (solid lines) and $\lambda_{\text{pump}} = 800\,\text{nm}$ (dashed lines). Accordingly, the dashed red line corresponds to Table 4.1(a).

for the smallest amount of absorbed energy of $u_L = 54\,\text{J}\,\text{cm}^{-3}$. Furthermore, the increase is stronger for the higher wavelength of 800 nm and thus the smaller photon energy. This can be understood, as absorption ratios presented in Fig. 3.3a do not vary greatly with the underlying DFT-DOS, but the amount of photons is bigger for the smaller photon energy at a fixed total energy.

The opposite relation is found for the data in Fig. 4.5, where the clean band gap of the parabolic-DOS dominates the behavior. Consequently, the higher amount of photons can not excite d-electrons to the sp-band, which is expressed by the very low interband absorption ratio. However, an increase in the sp-densities can be seen for higher absorbed energies, as the laser stimulated temperature increase creates free sp-states below Fermi energy and thus also increases the interband absorption ratio during laser-excitation time. This effect is presented in Fig. 4.6b. However, the interband absorption ratio decreases for the initially high ratios based on the DFT-DOS and the wavelength of 400 nm in the parabolic-DOS description. This is shown in Fig. 4.6 The remarkable influence of the underlying DOS becomes very clear in these comparisons.

Taking even higher laser energies into account in Fig. 4.7, the density increase shifts in comparison of 400 nm and 800 nm pulses, to the situation observed in Fig. 4.4, even for the parabolic-DOS, with almost no initial interband absorption ratio.

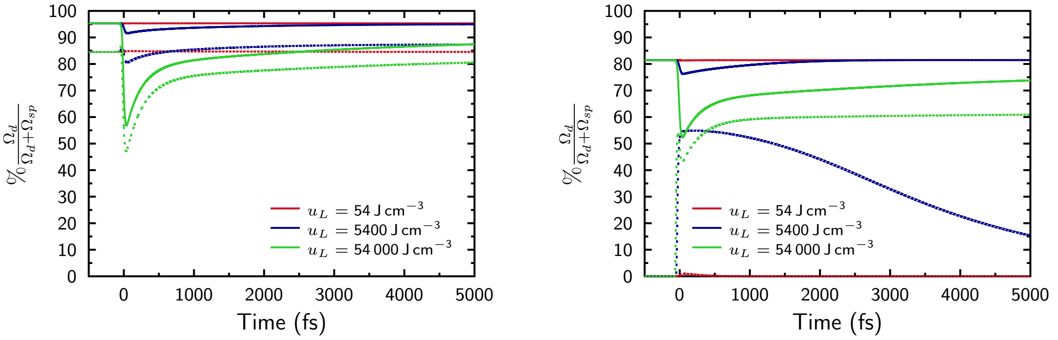

(a) DFT-DOS

(b) Parabolic-DOS

Figure 4.6: Simulated interband absorption ratios for different total absorbed laser energies u_L, an electron-electron relaxation time of $\tau_{\text{relax}} = 258\,\text{fs}$ and laser wavelengths of $\lambda_{\text{pump}} = 400\,\text{nm}$ (solid lines) and $\lambda_{\text{pump}} = 800\,\text{nm}$ (dashed lines). Accordingly, the dashed red line corresponds to Table 4.1(a) and the solid green line to Table 4.1(b).

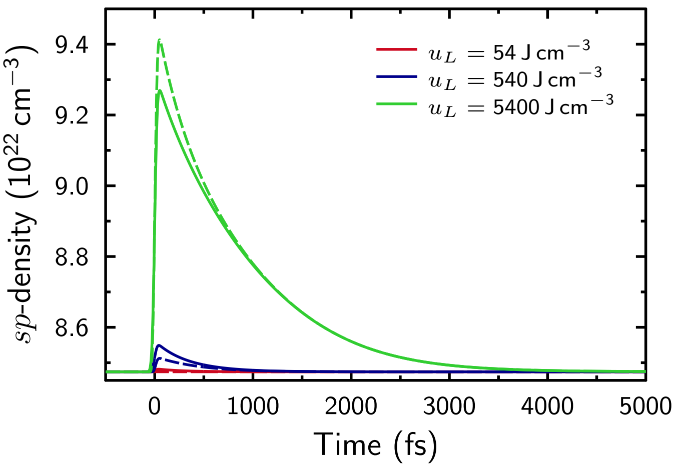

Figure 4.7: Simulated sp-band densities n_{sp} for different total absorbed laser energies u_L, based on the parabolic-DOS, for an electron-electron relaxation time of $\tau_{\text{relax}} = 258\,\text{fs}$ and pump pulse wavelengths of $\lambda_{\text{pump}} = 400\,\text{nm}$ (solid lines) and $\lambda_{\text{pump}} = 800\,\text{nm}$ (dashed lines). Accordingly, the dashed red line corresponds to Table 4.1(a) and the solid green line to Table 4.1(b).

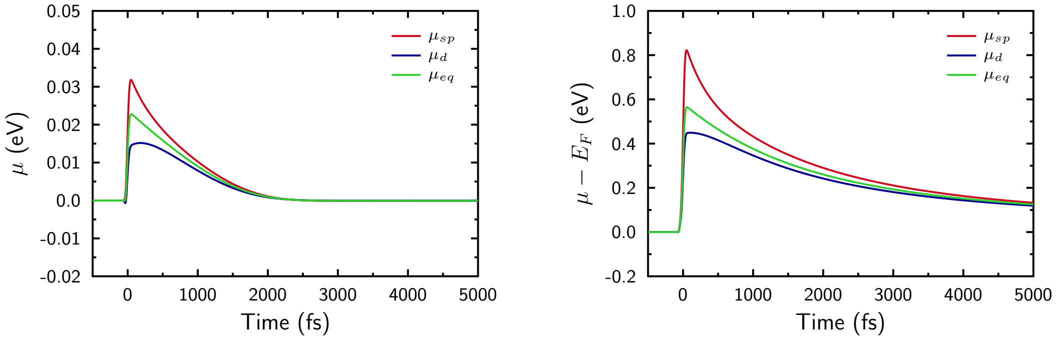

(a) Parameters from Table 4.1(a)

(b) Parameters from Table 4.1(b)

Figure 4.8: Simulated chemical potentials μ, compared for *sp*-band, *d*-band and the equilibrium case, based on DFT-DOS, for pump pulse parameters from Table 4.1(a) in (a) and from Table 4.1(b) in (b).

4.2 Chemical potential

The non-equilibrium in chemical potential between *d*- and *sp*-band is immediately connected to the band occupation non-equilibrium. In the Figs. 4.8, we see a strong dependence of the chemical potentials and their relaxation behavior of pump pulse parameters. In Fig. 4.8b, the chemical potentials rise to higher maximum values, than in Fig. 4.8a. The higher energy input leads to more electron excitations to higher energies. The change in temperature alone does not yield plenty available states in the statistical description, due to the smaller DOS at higher electron energies. Hence, the chemical potential rises in order to give the correct number of occupied electron states and comply electron number conservation.

Out of equilibrium, the *sp*-chemical potential is always bigger than the *d*-band chemical potential. The equilibrium chemical potential naturally is in between those two at all times. The above equilibrium *sp*-chemical potential corresponds to the increase in *sp*-band occupation density. Yet, in the total thermodynamic equilibrium, the equilibrium chemical potential and temperature differ from their initial values. Thus, the equilibrium *sp*-band occupation density also changes independent of the chemical potential non-equilibrium, due to the complex DOS relation between *d*- and *sp*-bands. But the huge initial changes of n_{sp} in Fig. 4.4 are strongly connected to chemical potential non-equilibrium.

4.3 Electron-lattice interaction

Fig. 4.9 shows the electron and lattice temperatures for both parameter sets from Table 4.1(a) and from Table 4.1(b). However, the laser pump pulse wavelength should not have any influence on the temperature development, if the absorbed energy density is

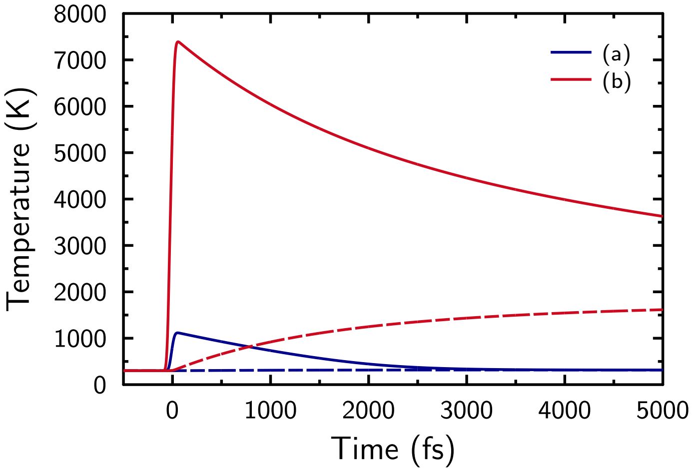

Figure 4.9: Simulated electron temperatures T_e (solid lines) and lattice temperatures T_i (dashed lines), for pump pulse parameters from Table 4.1(a) and Table 4.1(b), based on the DFT-DOS.

the same for both lasers. Laser energy resolved data is presented in Fig. 4.10. Both maximum electron temperature and equilibrium temperature increase, with increasing laser energy, as expected. Note, that the electron temperatures at high energy inputs are above the melting temperature of copper, which is located at $T = 1356\,\mathrm{K}$ [32]. However, in terms of phase transitions, the relevant temperature is that of the lattice, which defines the sample structure. Yet, we see ion temperatures rising above this threshold towards equilibrium for the parameters from Table 4.1(b) in Fig. 4.9.

4.4 Summary

We have presented results for the two-band electron distribution model in this chapter. The results have been based on simulations as introduced in Chapter 3. We have found relevant implications and limitations to the model. We have seen, that the model is limited by the accuracy of the numeric calculations and fails to calculate properties of copper for low photon energies, due to calculations with quasi zero values. On the other hand, the model has achieved to yield properties like temperature, electron occupation and chemical potential in a consistent and well understandable way. With a systematic investigation of the influence of the absorbed laser energies, we have found, that the DOS on which the calculations are based, has a strong impact on the relationships between the discussed quantities.

We will now introduce a model for optical properties of the copper sample based on the parameters discussed in this chapter.

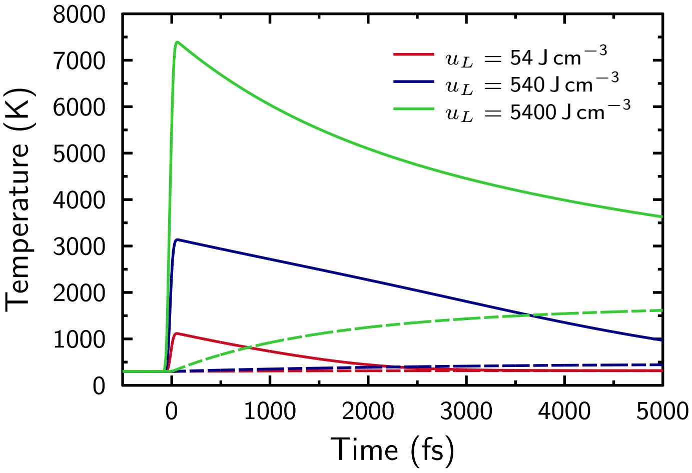

Figure 4.10: Simulated electron temperatures (solid lines) and lattice temperatures (dashed lines), for different total absorbed laser energies u_L, based on the DFT-DOS.

5 Optical Properties in the Drude Formalism

It is essential to verify theoretical calculations and models with measured experimental data. On the investigated ultrashort timescales and under the enormous heating, optical probing is very convenient for collecting experimental data. Especially with the technique of pump-probe experiments, optical data for copper under laser-excitation is available [5]. The probe pulse, that follows the pump pulse is of lower power, such that its influence on the material properties during probe time is minimized. Other techniques that involve for example attached connections are only applicable to solids. Furthermore, the optical investigations can be executed with the same setup, as for excitation.

Using the modeled data on electronic band occupations, we will see, that the dielectric function discussed in Section 2.4, can be calculated from there. On that basis, directly measured optical quantities can be calculated at any given time of the simulation. This allows for the comparison of simulation output with the real world. It would on the other hand, be also possible, to determine for example the dielectric function by fitting to experimental data and compare the dielectric functions. It is however more exact, to use as few free fit parameters as possible, as these can absorb errors in the model, sometimes even though a direct verification of the modeled quantities might not be possible.

5.1 Generalized Drude-Lorentz Model

In order to compare data with optical measurements, the most fundamental optical function, the dielectric function, has to be calculated first. The Drude and Lorentz models for the calculation of complex permittivity have been introduced in Section 2.4. Copper as a metal has both conduction electrons and bound states at deeper energy levels. In order to include all possible oscillations, a generalized Drude-Lorentz model is used. Its dielectric function ϵ^G (G for generealized), is defined as

$$\epsilon^G(\omega) = \epsilon_\infty + \epsilon^D(\omega) + \epsilon^L(\omega), \tag{5.1}$$

where $\epsilon^D(\omega)$ is given by Eq. (2.18) and $\epsilon^L(\omega)$ by Eq. (2.16). The term ϵ_∞ denotes for mixed effects, mainly of resonance frequencies way above the relevant spectrum of frequencies, that are not included separately, but make up for merely a constant effect in the lower frequency range. The index infinity is used, because it accords for way higher resonance frequencies $\omega \to \infty$. This term is often used as a fit parameter as well in the pure Drude or Lorentz model, for the same reason. While these formulations should hold true for any beam of incident light, it is here considered in the context of the probing light as $\omega = \omega_{\text{probe}}$.

With this formulation, the parameters used in the Drude and the Lorentz part, have to be determined depending on the current state. Here, a fundamental difference in the way of calculating the optical quantities compared to the quantities calculated with the model of rate equations, is found. In both cases, the objective is to determine properties of the heated copper sample at a given time, on small timescales. With the rate equations, this is achieved by tracing the change of the system numerically from the moment of excitation onward. For the optical properties, every time step is equally well described, but the calculation is not based on rate equations that model the time-development. Therefore, the state at every single moment, could as well be described without knowing the optical properties at any other given moment. However, as the underlying system develops continuously, a connection between different optical properties at different times is indeed expected. As a result of this behavior, the parameters of the dielectric function are not calculated by their evolution in time, but have to be known for any possible state of energy distribution.

For the Drude part in Eq. (2.18), the effective free-electron mass is the mass of $4sp$-electrons $m_e^* = m_{sp}$. This is taken from experiments to be $m_{sp} = 1.49 \cdot m_e$ [33]. Consequently, the free-electron oscillator strength f_0 can be determined as, $f_0 = \frac{m_e}{1.49 \cdot m_e} = 0.671$, following Eq. (2.19).

In accordance with the density and temperature rate equation model in Chapter 3, we restrict our model to the description of $4sp$- and $3d$-electrons, as optical oscillators. The oscillation of an electron implies an additional energy, transferring the electron to a different energy level. This transition is only possible if the excited state exists and is free. Hence the lower states with their huge band gaps are again of little importance, as the considered probe photon energies are in the NIR or visible range. In this consideration, the $3d$-electrons mainly below Fermi energy are the bound ones, while the $4sp$-electrons are considered free. Hence the free electron density n_{free} used for calculating the plasma frequency is set to be equal to the $4sp$-electron density, $n_{\text{free}} = n_{sp}$. Due to their dominating form of transition, the part of the bound d-electrons of the dielectric function, and hence the Lorentz part is sometimes also called the inter-band part of the dielectric function. Similarly, the Drude part is sometimes called the intra -band part of the dielectric function.

The dielectric function of copper at a temperature of 300 K is known through experiments [34]. The parameters ϵ_∞, the resonance and the damping frequencies and the oscillator strengths can be extracted by fitting the curve. The plasma frequency can be well calculated using Eq. (2.17). The use of well established formula is considered more accurate, than having a lot of free fit parameters, as they are basically adjusted such,

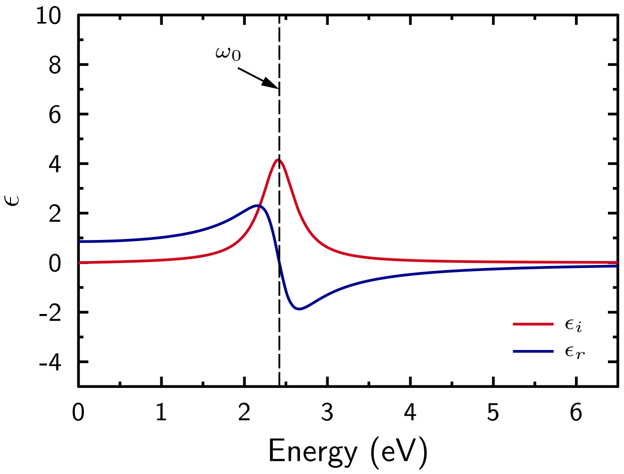

Figure 5.1: Real and imaginary part of dielectric function ϵ for one Lorentz term (with values from Table 5.1 for $j = 1$).

that the model fits the expectations. This leaves a lot of space for errors and many fit parameters are used already. For the Lorentz formalism, it does not matter, whether f_j or $s_j := f_j \cdot \omega_p^2$ is fitted, as a different value of the plasma frequency would just lead to a different fit value of f_j. For simplicity s_j is being used as free fit parameter for this part of the equation.

5.2 Fitting the Parameters of the initial Dielectric Function

Each term of the Lorentz dielectric function represents a characteristic peak in the permittivity around the respective resonance frequency, as represented exemplary in Fig. 5.1. In real metals like copper, the characteristic Lorentz curve peaks, are not necessarily well identifiable, as different resonances overlap in the frequency spectrum. In order to fit such curves with the Drude-Lorentz model without knowing the number of Lorentz terms $j_{\max}$, several models have been introduced [16, 35, 36]. The general approach is to pick an arbitrary, but not too high number of Lorentz poles [35], as the physical meaning of resonance terms would get lost with an increasingly high amount of terms [36]. There, the another problem is that with more terms more free fit parameters allow for fitting basically anything. Silaeva et al. [16] analyze, that four interband terms are sufficient to describe various transition metals. Following the analysis of Sehmi et al. from Ref. [35], we pick $j_{\max} = 4$ Lorentz terms to fit the dielectric function of copper. Indeed, we fit the same data from Ref. [33] at 300 K and in a similar fashion, we consider real and imaginary part of the permittivity

$$\epsilon = \epsilon_r + i\epsilon_i, \tag{5.2}$$

separately. As ϵ is complex, it can be split into a real part ϵ_r and an imaginary part ϵ_i. This can be done for every part of a sum individually and thus individually for the Drude term and the Lorentz terms. The split up results immediately from $1/z = \bar{z}/z\bar{z}$ for a complex number z, as

$$\epsilon_r^D(\omega) = f_0\omega_p^2 \frac{\omega^2}{\omega^2(\omega^2+\nu_{\text{total}}^2)}, \tag{5.3}$$

$$\epsilon_i^D(\omega) = f_0\omega_p^2 \frac{\omega\nu_{\text{total}}}{\omega^2(\omega^2+\nu_{\text{total}}^2)}, \tag{5.4}$$

$$\epsilon_{r,j}^L(\omega) = s_j \frac{\omega_{0,j}^2-\omega^2}{(\omega_{0,j}^2-\omega^2)^2+(\omega\Gamma_j)^2}, \tag{5.5}$$

$$\epsilon_{i,j}^L(\omega) = s_j \frac{\omega\Gamma_j}{(\omega_{0,j}^2-\omega^2)^2+(\omega\Gamma_j)^2}, \tag{5.6}$$

following from Eqs. (2.16) and (2.18), with r as subscript for the real and i for the imaginary part. For the Lorentz part the additional index j displays, that this is true for all the individual j_{max} terms of the sum in Eq. (2.16). The term ϵ_∞ is real and thus exclusively contributes to ϵ_r. Eq. (5.3) is true for all temperatures, but applied here for the equilibrium situation at 300 K.

We fit only the real part of the dielectric function, that contains all the free parameters, including ϵ_∞. Fitting the imaginary part as well will be discussed in Section 8.3. The beforehand determined values for plasma frequency Eq. (2.17), free-electron oscillator strength Eq. (2.19) and total free-electron scattering rate Section 5.3 are fixed to their calculated values. The plasma frequency follows as $\omega_p = 10.810\,\text{s}^{-1}$, with $n_{\text{free}}(300\,\text{K}) = 1/V$ from Eq. (3.3) for the free $4sp$-electrons. The data from Ref. [33] contains the usual refractive indices n and extinction coefficients κ. The imaginary part of the dielectric function is calculated out of these, using the squared version of Eq. (2.24) and isolating the imaginary part of the permittivity, given that $\mu \approx 1$. The resulting fit parameters are presented in Table 5.1. Additionally, the

Table 5.1: Fit parameters for dielectric function of copper in equilibrium situation at $T = 300\,\text{K}$.

j	s_j^{in}	$\hbar\omega_{0,j}^{in}$ in eV	$\hbar\Gamma_j^{in}$ in eV
1	5.000	2.421	0.500
2	5.000	2.883	0.623
3	14.572	3.680	1.000
4	25.000	4.943	1.260

fit yields $\epsilon_\infty = 3.652$. Fig. 5.2 shows the real and imaginary permittivity extracted from Ref. [33] and the fitted curves, with the parameters from Table 5.1. The fit parameters are determined using Gnuplot [37]. The fit parameters are restricted to

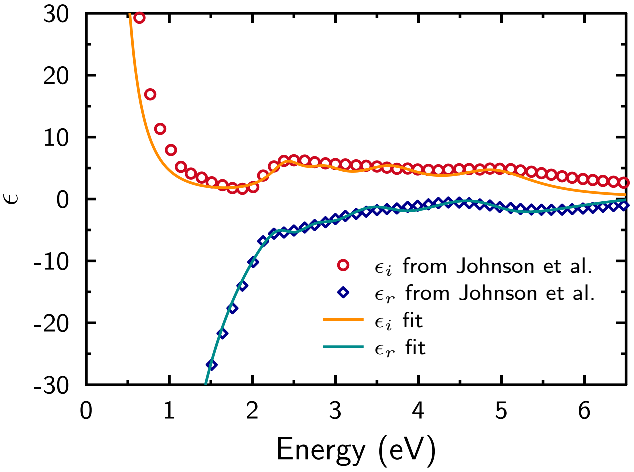

Figure 5.2: Real and imaginary part of dielectric function ϵ for different probe frequencies ω at 300 K from Ref. [33] and curves fitted with Gnuplot.

limited ranges, to assure, that the fitted curve matches the experimental data and that the fit values make sense in the context of physics. This limitation is assured by applying an arcustangens-like function on the actual fit parameters a, as follows

$$p(a) = \frac{p_{\max} - p_{\min}}{\pi}(\arctan(a) + \frac{\pi}{2}) + p_{min}. \tag{5.7}$$

Here $p(a)$ are the final fit parameters presented in Table 5.1, while a is actually being fitted. $p_{\max}$ is the maximum possible value for $p(a)$ and $p_{\min}$ the minimum possible value. In this context, the initial values of all fit parameters are chosen to be 0.1, as 0 would give the middle of the range of possible values $p(0) = (p_{\max} - p_{\min})/2$, but the program only works with non-zero values. $p(0.1) = ((p_{\max} - p_{\min})/2) \cdot 1.063$ is a good starting point for optimization, because it describes a value close to the middle of all possible values.

5.3 Temperature-dependent development of Drude parameters

Based on the previous analysis, the only parameter, that remains to be determined for non-equilibrium conditions, in the Drude model is the total electron scattering frequency ν_{total}. According to Eq. (2.20), it is composed of the electron-phonon scattering frequency and the electron-electron scattering frequency.

Here, we suggest two different methods, to describe those frequencies. The formulation of Fourment et al. [38] is based on measurements for gold, but the analysis is universal for noble metals. In that approach, the scattering can be described with the equations

$$\nu_{ei}(T_i) = BT_i, \tag{5.8}$$

$$\nu_{ee,F}(t) = A_F n_d(t)[n_d^{\text{full}}(t) - n_d(t)]. \tag{5.9}$$

The electron-phonon scattering frequency Eq. (5.8) is proportional to the lattice temperature T_i. The constant of proportion can be extracted from measurements at $300\,\text{K}$, via $B = \nu_{ei}^{\text{cold}}/300\,\text{K}$, where $\nu_{ei}^{\text{cold}} = 0.145\,\text{fs}^{-1}$ is the electron-phonon scattering frequency for cold copper [33]. The measured data has a statistical uncertainty. However, we consider the uncertainty to be much smaller than the errors arising from approximations in the formulation of the model.

The electron-electron scattering frequency Eq. (5.9) is described to be proportional to the density of $3d$-electrons $n_d(t)$ and of $3d$-holes $n_d^{\text{full}} - n_d(t)$, where n_d^{full} is the density of $3d$-electrons, when the $3d$-band is fully occupied. Hence, n_d^{full} equals $10/V$ with the unit cell volume V. This equals the initial d-band occupation, such that there are no holes and no initial electron-electron scattering. As we consider particle conservation, the number of d-band holes equals the number of excited sp-electrons. According to Fourment et al., the d-d and the sp-sp scattering do not play an important role, such that the scattering between d- and excited sp-electrons dominates the electron-electron scattering. The proportion described by A_F is almost constant for gold at elevated temperatures. The method of Fourment et al. directly connects to the band occupation densities and gives a good operational description of the processes, but no constant of proportion for copper is known. We will determine the constant via comparison with the second method.

For this second method we use the formulation for the application on copper by Kirkwood et al. [11]. The electron-phonon scattering frequency is determined in an equivalent manner, as in Eq. (5.8), while the electron-electron scattering is specified by

$$\nu_{ee,K}(T_e) = \frac{A_K k_B}{\hbar T_F} T_e^2, \tag{5.10}$$

where T_F is the Fermi temperature and the proportionality A_K is determined by Kirkwood et al. to be equal to 3. This formula however is independent of the electron band occupation densities, but directly depends on the electron temperature. An additional limitation to the total scattering frequency is introduced as

$$\nu_{\text{total,K}} = min[\nu_{ei} + \nu_{ee,K}, \nu_c], \tag{5.11}$$

$$\text{with } \nu_c(T_e) = \frac{\sqrt{v_F^2 + \frac{k_B T_e}{m_e}}}{r_0}. \tag{5.12}$$

There ν_c is the critical frequency and such the maximum possible collision frequency, that follows from the condition, that the ion sphere radius r_0 cannot be bigger than the electron mean free path [11]. v_F is the Fermi velocity $v_F = \sqrt{2k_B T_F/m_e}$.

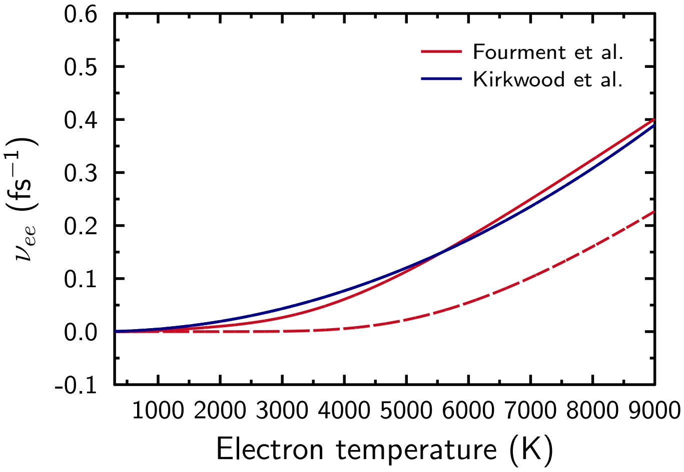

Figure 5.3: Equilibrium electron-electron scattering frequencies with method of Fourment et al. and Kirkwood et al. . For Fourment et al. the solid line is based on the DFT-DOS and the dashed line is based on the parabolic-DOS.

In the second approach, the electron-electron scattering is exclusively determined by the electron temperature. This is, because the description is made for equilibrium electron distributions. For our description of non-equilibrium electron distributions, the use of the first method is more appropriate. In order to determine its validity and to extract defining constants, we compare the equilibrium case to the second method. The equilibrium case can easily be traced, by using the beforehand calculated values of the equilibrium chemical potential in Chapter 3.

The application of $T_F = 8.16 \times 10^4\,\mathrm{K}$ [39], yields the electron-electron scattering curve in Fig. 5.3. There, it is compared to the equilibrium scattering frequency from the method of Fourment et al. . In this context, equilibrium means the equilibrium in chemical potentials and thus electron densities. The applied coefficient $A_F = 0.36\,\mathrm{fs}^{-1} \cdot V^2$ is the one for gold [38].

The curves for the DFT-DOS intersect each other, but are almost identical in the spectrum of relevant temperatures. The spectrum follows from the maximum electron heatings in Chapter 4. Thus, we apply the non-equilibrium description by Fourment et al., as it fits our situation better. The parameter for gold also describes the behaviour of copper well, in agreement with established models. We use the same model for the calculations on the parabolic-DOS. The parabolic-DOS, is introduced as a rough approximation to the actual energy distribution in copper, but with the expected d-band gap. It does not represent the actual electron distribution. This explains the huge deviation to the scattering with the DFT-DOS. The parabolic-DOS is mainly

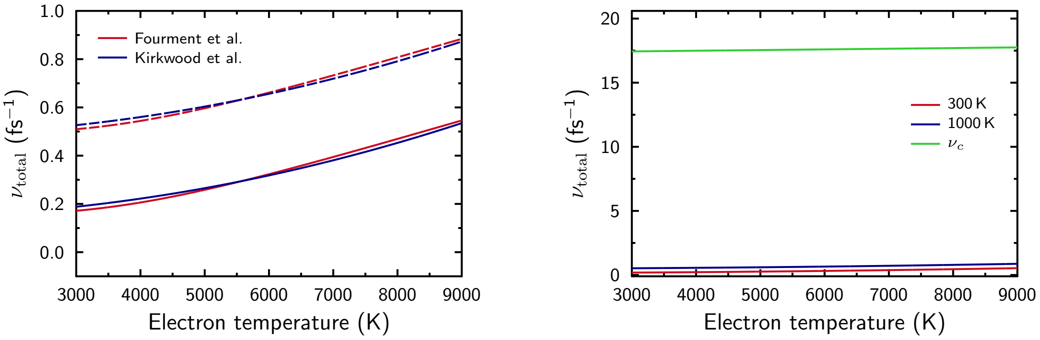

(a) Method Comparison

(b) Comparison with ν_c

Figure 5.4: Equilibrium total electron scattering frequencies with method of Fourment et al. and Kirkwood et al., based on the DFT-DOS. In (a) the continious lines represent lattice temperatures of 300 K and the dashed lines represent 1000 K of lattice temperature. In (b) the results of the Kirkwood method are compared with the critical collision frequency.

discussed, as to observe the influence of the band gap and the DOS on the results of the simulation. Hence we expect to observe the actual electron scattering behavior in connection with the DFT-DOS and thus base our further discussion of electron scattering behavior on this. Even though it might seem so in Fig. 5.3, the electron scattering values for the parabolic-DOS do not drop below zero, which is physically impossible.

The total electron scattering frequencies are determined as $\nu_{\text{total}}(T_i, T_e) = \nu_{ei}(T_i) + \nu_{ee}(T_e)$ [Eq. (2.20)] and are presented in Fig. 5.4. The influence of the lattice temperature as the curve offset is indeed relevant for the total scattering. In Fig. 5.4b, it can be seen, that the critical frequency does not impose a relevant limitation to electron scattering in the discussed temperature and hence laser energy range. The displayed electron and ion temperatures are chosen such, that the ion temperatures are below the melting temperature of copper of $T = 1356\,\text{K}$ [32] and the electron temperatures are bigger than the ion temperatures.

Fig. 5.5 shows the time-development of the total electron scattering frequency for an excitation of copper with the pump pulse parameters from Table 4.1(a) and from Table 4.1(b). Prior to the laser-excitation, it is constant, as the temperature is in constant equilibrium. Due to Pauli blocking of the $3d$-excitation to $4sp$-states, electron-electron scattering is prevented at first and the initial scattering contribution is mainly due to electron-phonon scattering. At laser heating, the total scattering rapidly increases, dominated by the increase in electron-electron scattering. After that initial elevation, the electrons cool down, while the ions are heated up. Consequently,

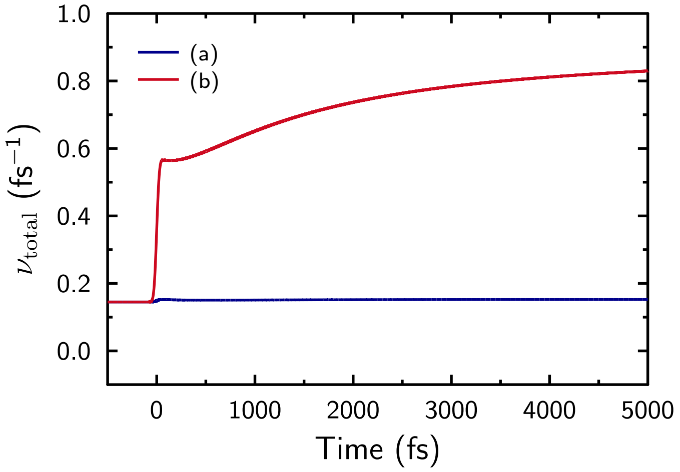

Figure 5.5: Non-equilibrium total electron scattering frequencies with method of Fourment et al., for pump pulse parameters from Table 4.1(a) and Table 4.1(b), based on the DFT-DOS.

the scattering rates change in opposite directions to each other and electron-phonon scattering gains importance again.

Under non-equilibrium band occupations, the electron scattering becomes time-dependent, rather than temperature dependent, as described at the end of Section 2.4. We demonstrate this in this context representatively for all Drude-Lorentz parameters in Fig. 5.6. Starting at 300 K, the electron-electron scattering initially rises with the electron temperature. Consequently, the electronic distribution changes with time, such that the scattering decreases on a different path, while the electrons cool down through coupling to the lattice.

The difference in total electron scattering for different electron temperatures before and after reaching the maximum electron temperature is even higher, as can be seen in Fig. 5.7. There, the lattice heats, while the electrons cool down, which consequently increases the electron-ion scattering rate.

5.4 Temperature-dependent development of Lorentz parameters

To model the fitted parameters at different electron temperatures, a set of modifying equations for different underlying conditions is developed. The idea of the model relies

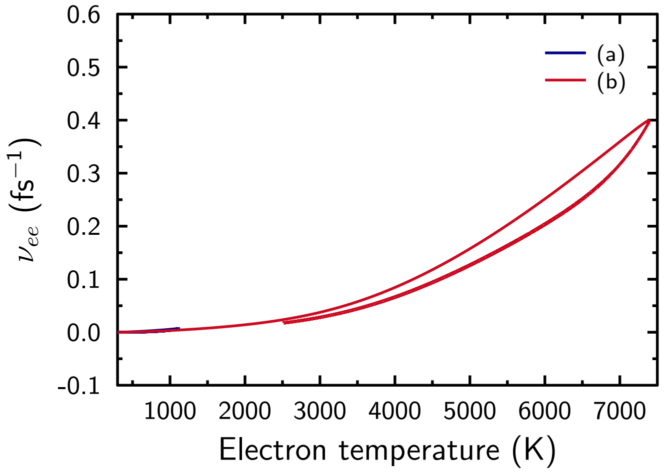

Figure 5.6: Non-equilibrium total electron scattering frequencies with method of Fourment et al., for pump pulse parameters from Table 4.1(a) and Table 4.1(b), based on the DFT-DOS. The values are calculated for a time interval from $t = -1\,\text{ps}$ to $t = 10\,\text{ps}$.

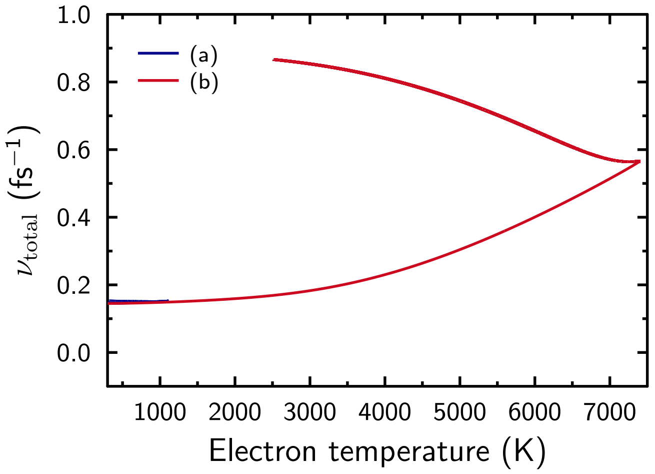

Figure 5.7: Non-equilibrium total electron scattering frequencies with method of Fourment et al., for pump pulse parameters from Table 4.1(a) and Table 4.1(b), based on the DFT-DOS. The values are calculated for a time interval from $t = -1\,\text{ps}$ to $t = 10\,\text{ps}$.

on the quantum mechanical relation [Eq. (2.2)]

$$E = \hbar\omega. \tag{5.13}$$

Based on that, frequencies ω correspond to and can be mathematically converted to energies E and vice versa. With this connection in mind, the possible electron oscillations, should be restricted by Pauli blocking as well. This is because the oscillation would give an additional energy to the electron, that can only be absorbed if the states at the energy elevated by $\hbar\omega$ are at least temporarily available. Furthermore, the influence of every term in the Lorentz dielectric function is particularly strong for frequencies close to the respective resonance frequency. Thus we model the variation in one oscillator strength with the availability of electrons that can absorb the respective photon energy at the terms resonance frequency.

For the Lorentz part at the advent of the probe pulse, the $3d$-electrons are the ones that can perform bound oscillations and the analysis is hence restricted to those. Pauli blocking for energies below chemical potential is very high and for energies close to or above the chemical potential, the availability of $3d$-electrons is rather low.

Based on these prerequisites, we model the oscillation strength of each term as depending on the electron density in a small confined energy area around the energy of $E_F - \hbar\omega_{0,j}$. At $T_e = 300\,\mathrm{K}$ a stimulation with more or less the resonance frequency would then lead to an excitation to Fermi energy, where the Fermi energy describes the first energy level with at least half of the energy states available. This apparently excludes a lot of other electrons, that are available for photon energy absorption at those resonance energies, but it gives a consistent way, to describe different resonance frequencies separately and most importantly makes the same assumptions for all the terms. Still, the terms change differently relative to each other and various areas of the energetic electron distribution are being connected to specific oscillations. This mapping of the Lorentz terms to the d-band energy distribution is shown in Fig. 5.8.

Indeed the influence of other electronic energies than the selected ones should be smaller to the dielectric function or compensate each other. For lower electron energies, the final states would be below Fermi energy and thus highly restricted by Pauli blocking. For higher energies on the other hand, the Fermi distribution decreases faster with rising electron temperature. Very high resonance frequencies may allow for a wider energetic range of electrons to be excited above Fermi energy. If the temperature rises, both high and low energy resonances lose electrons in the initial area, but the lower ones with higher initial electron energies lose relatively more of their total absorbing electrons. This is because, the energetically deeper states remain little excited for the high resonance frequencies.

The modeled equations for the three free parameters in the dielectric Lorentz

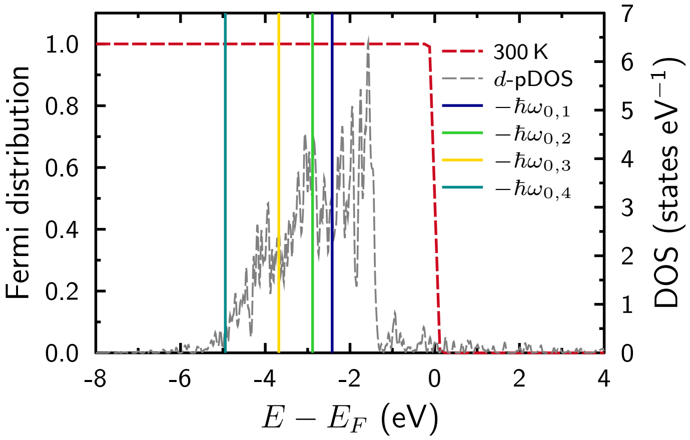

Figure 5.8: d-band pDOS, Fermi distribution and energies $\hbar\omega_{0,j}$ at $T = 300\,\mathrm{K}$.

function read

$$f_j(t) = f_j^{in} \frac{n_d(\omega_{0,j}^{in}, T_e(t))}{n_d(\omega_{0,j}^{in}, 300\,\mathrm{K})}, \tag{5.14a}$$

$$\omega_{0,j}(t) = \omega_{0,j}^{in} + \frac{\mu_{sp}(t) - \frac{1}{2}k_B T_e(t) - [E_F - \frac{1}{2}k_B 300\,\mathrm{K}]}{\hbar}, \tag{5.14b}$$

$$\Gamma_j(t) = \Gamma_j^{in} + \nu_{ee}(t). \tag{5.14c}$$

All three Eqs. 5.14 are based on their initial value at $T_e = 300\,\mathrm{K}$. These are the values fitted to the initial dielectric function in equilibrium and are marked with superscript *in* for initial.

The aforementioned variation in the oscillator strength is modeled with Eq. (5.14a). The initial oscillator strength f_j^{in} is multiplied by the ratio of $3d$-electron density $n_d(\omega_{0,j}, t)$ around the energy of $\hbar\omega_{0,j}^{in}$ below Fermi energy at the given electron distributions at time t divided by the equivalent $3d$-electron density $n_d(\omega_{0,j}, 0\,\mathrm{fs})$ at the initial conditions. This electron density around a certain energy is described similarly to Eq. (3.2) via

$$\begin{aligned} n_d(\omega_{0,j}, t) &= \int_{E_{\min}^j}^{E_{\max}^j} dE \cdot f(E, \mu_d(t), T_e(t)) \cdot D(E) \\ &= (E_{\max}^j - E_{\min}^j) \cdot f(E^j(t), \mu_d(t), T_e(t)) \cdot D(E^j(t)), \end{aligned} \tag{5.15}$$

with $E^j(t) \in [E_{\min}^j, E_{\max}^j]$, where $[E_{\min}^j, E_{\max}^j]$ is small and includes $E_F - \hbar\omega_{0,j}$. The second equality in Eq. (5.15) is true because of the mean value theorem (MVT) for small intervals $[E_{\min}^j, E_{\max}^j]$. The temperature dependence of E^j simply follows from the temperature dependence of n_d, as the mean value theorem would in general give a different value of E^j for every integral. With this equation and the further approximation of $E^j(t) = E_F - \hbar\omega_{0,j}^{in}$ for all electron temperatures including $T_e = 300\,\mathrm{K}$, Eq. (5.14a) reduces to

$$\begin{aligned} f_j(t) &= f_j^{in} \frac{f(E_F - \hbar\omega_{0,j}(t), \mu_d(t), T_e(t))}{f(E_F - \hbar\omega_{0,j}^{in}, E_F, 300\,\mathrm{K})} \frac{(E_{\max}^j - E_{\min}^j)}{(E_{\max}^j - E_{\min}^j)} \frac{D(E_F - \hbar\omega_{0,j}^{in})}{D(E_F - \hbar\omega_{0,j}^{in})} \\ &= f_j^{in} \frac{f(-\hbar\omega_{0,j}(t), \mu_d(t) - E_F, T_e(t))}{f(-\hbar\omega_{0,j}^{in}, 0, 300\,\mathrm{K})}. \end{aligned} \tag{5.16}$$

with $\mu_d(300\,\mathrm{K}) = E_F$.

The second equation in Eqs. (5.14), Eq. (5.14b) describes the change in the resonance frequencies with electron temperature. The initial resonance frequencies $\omega_{0,j}^{in}$ are shifted by the frequency that corresponds to the difference of $\mu_{sp}(t) - \frac{1}{2}k_B T_e(t)$ to its initial value at $\mu_{sp}(0) = E_F$ and $T_e(0) = 300\,\mathrm{K}$. This term describes the chemical potential of the *sp*-states $\mu_{sp}(t)$ at elevated electron temperatures minus half the broadening $k_B T$ of the Fermi distribution function.

While in Eq. (5.14a) the investigated energy interval remains constant, the chemical potential changes with time. Thus the energy difference from $E_F - \hbar\omega_{0,j}^{in}$ to the chemical potential of the *sp*-states changes. In order to keep simulating excitations to the half filled *sp*-states around the *sp*-chemical potential, we adjust the resonance frequencies. The adjustment of the energy range in Eq. (5.15) would on the other hand lead to bad comparability of the electron availability, due to different DOS values.

Independent of the adjustments for the other two Lorentz parameters, Eq. (5.14c) describes the time-dependent damping frequency as the sum of the initial damping frequency Γ_j^{in} and the electron-electron scattering frequency $\nu_{ee}(t)$, described in Eq. (2.20). As described by Fourment et al., free $4sp$-electrons scatter with $3d$-electrons and vice versa. This is represented by the term $\nu_{ee}(t)$ in the damping frequency development, as the scattering produces an additional damping with the respective frequency. Indeed, there is no initial electron-electron scattering, according to Eq. (5.9). Effectively, scattering and damping can be treated equally in this context, as every damping can be described as some sort of scattering.

The modeling of Lorentz parameters in this manner is yet little investigated and slight changes in the modeling may lead to huge improvements in the final results.

5.5 Summary

In this chapter, we have described a method to calculate the dielectric function of copper, based on the parameters discussed in Chapter 4. Therefore, we have used a generalized Drude-Lorentz approach and have fitted the dielectric function of copper at our initial sample conditions. We have introduced a system to modulate the parameters of the dielctric function that are independent of the probe-frequency with time. There, we have derived the time-dependence of these parameters from the time-dependence of temperature and electron occupation densities.

In connection with the free electron scattering frequencies, we have found that the model for gold with non-equilibrium electron occupations from Fourment et al. [38] is also applicable for the description of copper.

In Chapter 6, we will present the resulting evolution of the dielectric function and values of reflectivity and transmissivity and compare them with the data by Obergfell et al. [5].

6 Transient Optical Properties in Copper

Based on the descriptions made in Chapter 5 and the formulae for calculating reflectivity and transmissivity from Section 2.5, we will now present the evolution of optical parameters and a comparison with the data by Obergfell et al. [5].

6.1 Time-development of the Dielectric Function

The time-development of both real and imaginary parts of the dielectric function is shown in Fig. 6.1 for different pump laser energies and probe pulse wavelengths. The amount of absorbed energy has a huge influence on the respective values. For high amounts of absorbed energies, the optical material response changes greatly. The differences for the absorbed energies of $u_L = 54\,\mathrm{J\,cm^{-3}}$ are rather low, but in the following section we will see, that this already leads to important changes of the material properties.

6.2 Reflectivity and Transmissivity

We now calculate the reflectivity and transmissivity, for the same material and laser parameters, as used by Obergfell et al. [5]. The properties of copper and the pump pulse have already been described in Chapter 3, and particularly in Section 3.3.

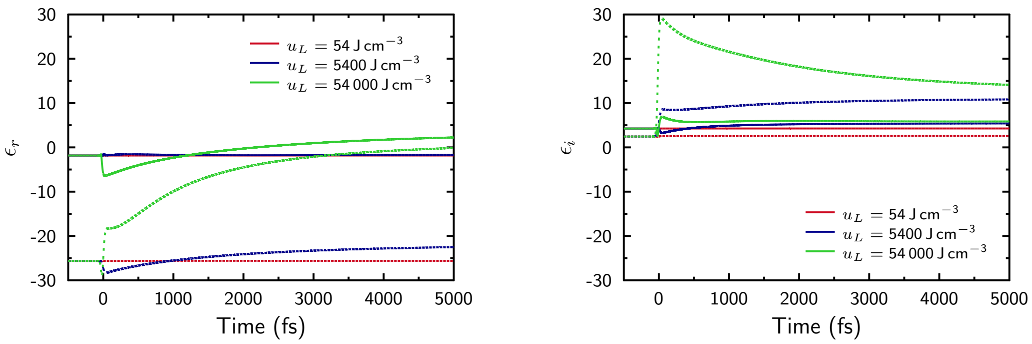

(a)

(b)

Figure 6.1: Simulated time-development of (a) real and (b) imaginary part of dielectric function for different total absorbed laser energies u_L and laser wavelengths of $\lambda_{\mathrm{probe}} = 400\,\mathrm{nm}$ (solid lines) and $\lambda_{\mathrm{probe}} = 800\,\mathrm{nm}$ (dashed lines), based on the DFT-DOS.

The pump laser properties used by Obergfell et al. have been introduced as the parameter set (a) in Table 4.1. For calculating the measurable optical quantities of reflectivity and transmissivity, some more information about the probe process is required.

The experiment is performed at an incidenct angle of $\theta_{\mathrm{sur}} = 7°$, with p-polarized light. At this condition, Eqs. (2.29c) and (2.29d) are used for calculating reflection and transmission coefficients.

The probe thickness of the copper film is $d = 24\,\mathrm{nm}$. The film is surrounded by vacuum, with $\epsilon_{\mathrm{sur}} = n_{\mathrm{sur}} = 1$. The film is applied on a 1 mm thick MgO substrate. This effectively creates a two-layer film, including another probe material. At both interfaces of copper-MgO and MgO-vacuum, the reflectivity differences in the investigated range of photon energies at normal incidence are sufficiently low, as to assume a free copper film. Interference inside the MgO film and the two-layer system is similarly little influenced by the MgO substrate, as not a lot of light is reflected at the MgO-vacuum interface in the first place. The copper-MgO reflectivity at a photon energy of 1.55 eV is $R = 93.97\,\%$, calculated via Eq. (2.32a) and Eq. (2.33) with data from Johnson et al. [33] for copper and Stephens et al. [40] for MgO, compared to the copper-vacuum reflectivity of 96.20 %. The corresponding MgO-vacuum reflectivity is $R = 7.12\,\%$. Similar differences are obtained for other NIR and visible photons.

We present the normalized maps of reflectivity and transmissivity changes for a range between probe pulse energies of 1.25 eV and 2.8 eV in Fig. 6.2, resulting from our simulations. The experimental results are also presented in Fig. 6.2 for comparison. The normalized values correspond to

$$\frac{\Delta R}{R}(\omega, t) = \frac{R(\omega, t) - R^{in}(\omega)}{R^{in}(\omega)}, \tag{6.1}$$

$$\frac{\Delta T}{T}(\omega, t) = \frac{T(\omega, t) - T^{in}(\omega)}{T^{in}(\omega)}, \tag{6.2}$$

with $R^{in}(\omega)$ and $T^{in}(\omega)$ as the reflectivity and transmissivity in equilibrium at $T_e = 300\,\mathrm{K}$. These initial values are the ones with the parameters fitted to the data of Johnson et al. [33] and hence corresponding to times before laser-matter interaction.

In Fig. 6.2, one can indeed guess maxima or minima around $\hbar\omega_{\mathrm{probe}} = 2.6\,\mathrm{eV}$ in reflectivity and transmissivity similar to those in the experimental data. But for the experimental data, these maxima and minima lie around $\hbar\omega_{\mathrm{probe}} = 2.1\,\mathrm{eV}$, which could be explained by the d-band energy gap, that has this exact size [5].

In Fig. 6.3, the results of the simulation are presented for a higher range of probe pulse frequencies between 1.25 eV and 3.6 eV. The extrema do indeed have a similar shape, as those determined by the experiment. Furthermore, a second pair of extrema can be seen at higher probe frequencies.

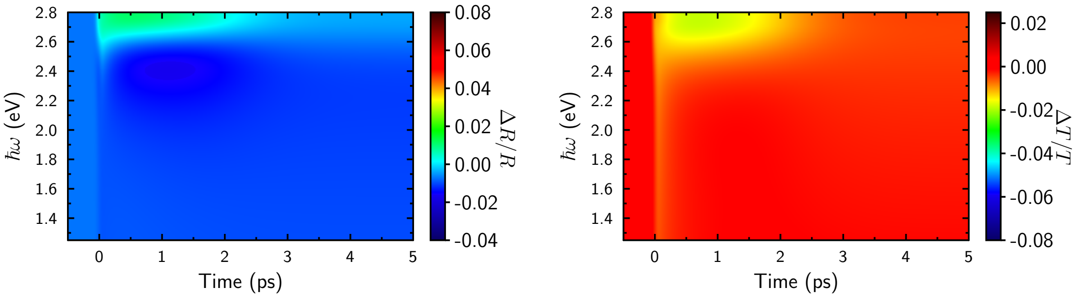

(a) Simulation, Reflection

(b) Simulation, Transmission

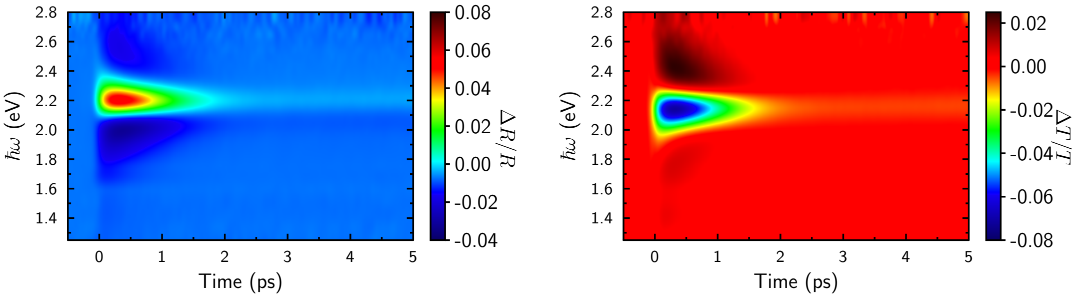

(c) Obergfell et al. [5], Reflection

(d) Obergfell et al. [5], Transmission

Figure 6.2: Normalized reflection and transmission differences at a 24 nm thick copper film resulting from two-temperature simulations, in comparison with experimental data by Obergfell et al. [5]. The values are based on the fitted initial Drude-Lorentz parameters in Table 5.1 and the DFT-DOS with the pump pulse parameter set from Table 4.1(a). The incidence angle is set to 7 degrees for *p*-polarized light.

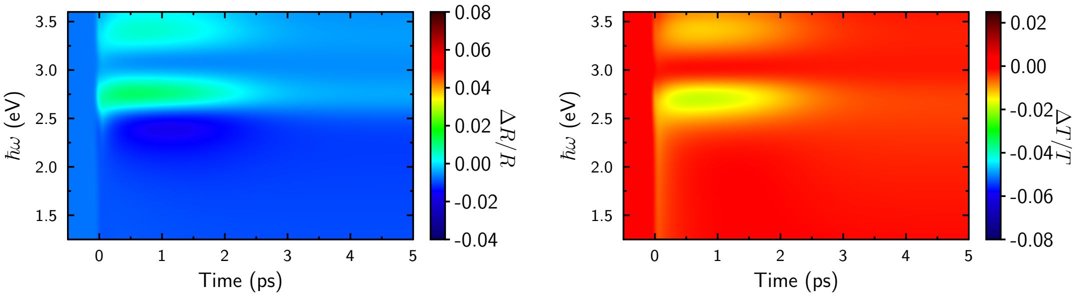

(a) Reflection

(b) Transmission

Figure 6.3: Normalized reflection and transmission differences at a 24 nm thick copper film resulting from two-temperature simulations. The input parameters are equal to those in Fig. 6.2, but with a bigger range of probe pulse enegy values.

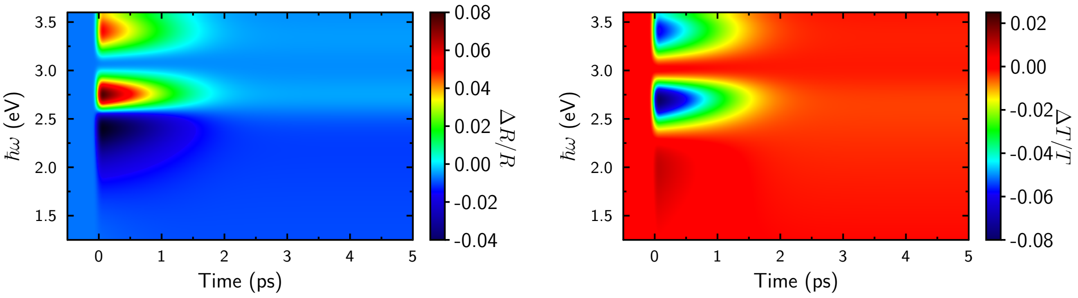

(a) Reflection

(b) Transmission

Figure 6.4: Normalized reflection and transmission differences at a 24 nm thick copper film resulting from two-temperature simulations. The input parameters are equal to those in Fig. 6.3, but based on the parabolic-DOS.

At this part, a notable attribute of the modeling of both Drude and Lorentz parameters is, that these parameters themselves are independent of the probe pulse frequency. Only in total, the dielectric function becomes frequency and time-dependent. However, we see great differences in the development of reflectivity and transmissivity with time, depending on the probe pulse frequency. This behavior is not modeled explicitly. Therefore the general similarity of the reflectivity and transmissivity maps already supports the model. This is even though the position of the maxima and minima and their amplitudes differ a lot from the experimental data. Further on, we will try to improve the simulated results, to fit the experimental data better, by varying some input parameters. This way, we can as well see the influence of different parameters.

In Fig. 6.4, the reflectivity and transmissivity maps are shown based on the parabolic-DOS. As the position of maxima and minima in the experimental data is around the *d*-band gap and the parabolic DOS implements the correct sharp *d*-band gap, a more accurate position of the extrema might be expected. However, the extrema are around the same positions, as for the DFT-DOS, but the amplitudes differ greatly and are more similar to the experimental ones.

Yet, consulting the underlying system of equations, the influence of the fitted Drude and Lorentz parameters on the final results should be of importance. Furthermore, the first two resonance frequencies lie around the positions of the extrema in reflectivity and transmissivity development. Hence, we introduce a new fit to the dielectric function, in order to check the influence of these parameters.

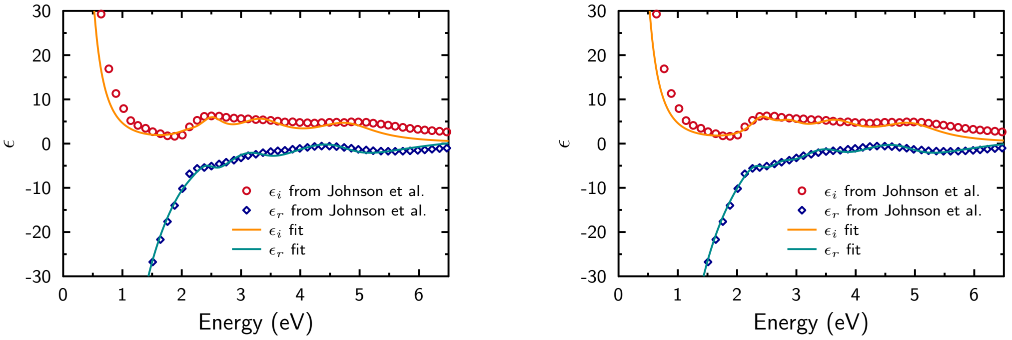

(a) $\hbar\omega_{0,j=1} = 2.1\,\text{eV}$ fixed

(b) free parameters

Figure 6.5: Real and imaginary part of dielectric function ϵ for different probe frequencies ω at 300 K from Ref. [33] and curves fitted with Gnuplot.

6.3 Fit of Initial Drude-Lorentz Parameters with Fixed Frequency

We fix the first resonance frequency to $\hbar\omega_{0,1}^{in} = 2.1\,\text{eV}$ and fit the other parameters in order to obtain a good approximation of the dielectric function. The fit is done in the same fashion, as in Section 5.2. The resulting Lorentz parameters are presented in Table 6.1 and we obtain $\epsilon_\infty = 3.756$. The obtained fit curves are shown in Fig. 6.5 and compared to the original ones from Fig. 5.2. As the amount of fitted parameters is very big, the curve could still be represented with similar precision, which justifies the use of these new initial parameters.

Table 6.1: Fit parameters with fixed first resonance frequency at $\hbar\omega_{0,j=1} = 2.1\,\text{eV}$, for dielectric function of copper in equilibrium situation at $T = 300\,\text{K}$.

j	s_j^{in}	$\hbar\omega_{0,j}^{in}$ in eV	$\hbar\Gamma_j^{in}$ in eV
1	0.924	2.100	0.500
2	5.000	2.515	0.499
3	15.000	3.260	1.000
4	25.000	4.795	1.266

The DFT-DOS based results represented in Fig. 6.6 have their first extrema rather around $\hbar\omega_{\text{probe}} = 2.3\,\text{eV}$. This is closer to the expected experimental images, without making any major changes in the model. Fig. 6.7 represents the same parameters, but based on the parabolic-DOS. It seems, that the simulated extrema are indeed strongly connected to the initial resonance frequencies of the Lorentz oscillations. The second set of extrema might result from the higher resonance frequencies. These resonance

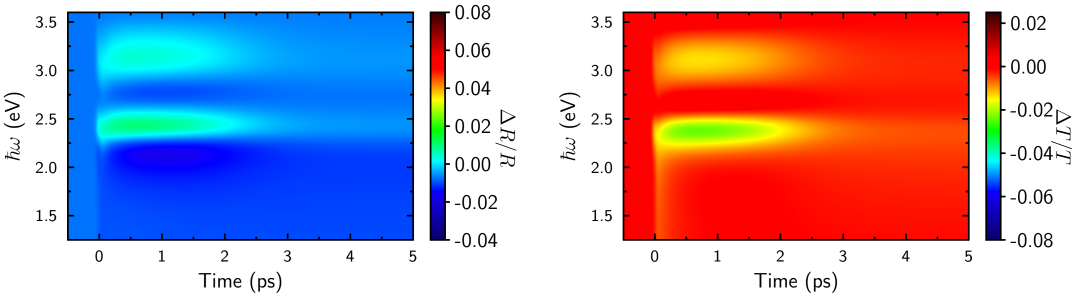

(a) Reflection (b) Transmission

Figure 6.6: Normalized reflection and transmission differences at a 24 nm thick copper film resulting from two-temperature simulations. The input parameters are equal to those in Fig. 6.3, except for the initial Drude-Lorentz parameters, which are taken from Table 6.1.

frequencies do not necessarily appear in this outstanding way in the dielectric function. They rather are modeled, in order to fit the function properly.

The low accuracy of the Drude-Lorentz fit might explain the deviation in the position of the extrema in the reflectivity and transmissivity maps, between our model and the experiment. The band gap however has little immediate influence on these positions regarding the DOS. Yet, the dielectric function of copper is connected to its d-band gap, such that the band gap influence is suppressed by inexact fitting.

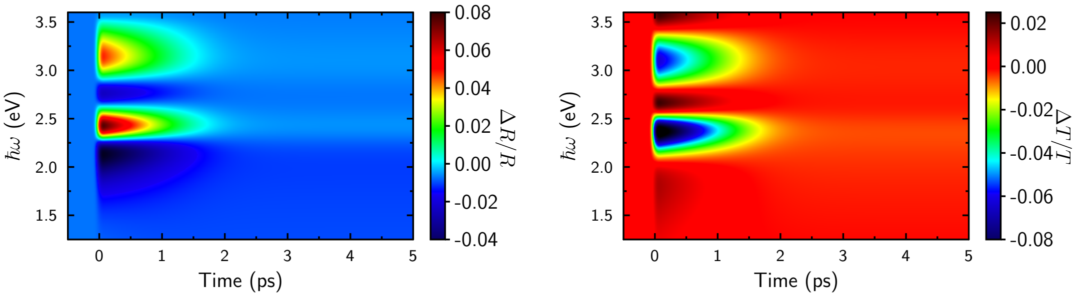

(a) Reflection (b) Transmission

Figure 6.7: Normalized reflection and transmission differences at a 24 nm thick copper film resulting from two-temperature simulations. The input parameters are equal to those in Fig. 6.3, except for the initial Drude-Lorentz parameters, which are taken from Table 6.1. Furthermore, the simulation is based on the parabolic-DOS.

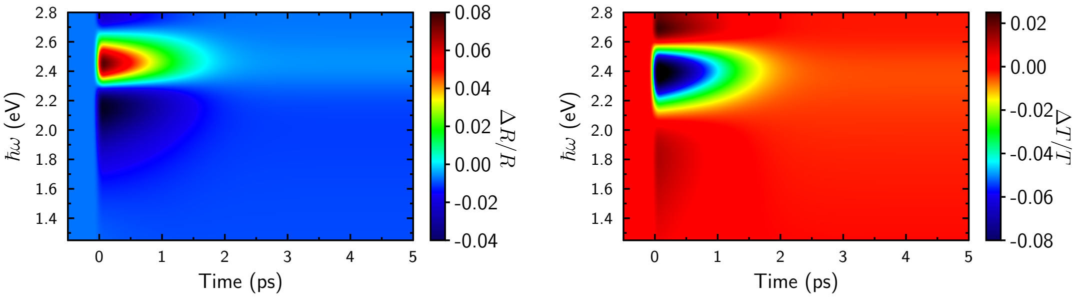

(a) Simulation, Reflection

(b) Simulation, Transmission

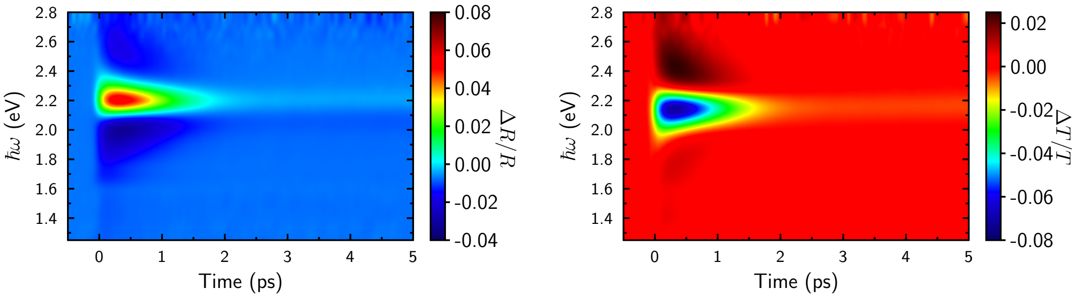

(c) Obergfell et al. [5], Reflection

(d) Obergfell et al. [5], Transmission

Figure 6.8: Normalized reflection and transmission differences at a 24 nm thick copper film resulting from two-temperature simulations, in comparison with experimental data by Obergfell et al. [5]. The values are based on the fitted initial Drude-Lorentz parameters with fixed frequency in Table 6.1 and the parabolic-DOS with the pump pulse parameter set from Table 4.1(a). The incidence angle is set to 7 degrees for p-polarized light.

A final comparison of the R- and T-maps with experimental data is given in Fig. 6.8, with the dielectric function for the fixed Frequency fit parameters from Table 6.1, based on the parabolic-DOS. These results do resemble the experimental data well, keeping minor inaccuracies due to fitting in mind. With the forced band gap energy in both the underlying DOS and the fit to the dielectric function, this is the simulated result closest to the experiment.

6.4 Summary

In this chapter, we have presented results for the optical properties of reflectivity and transmissivity and the dielectric function itself. We have shown a strong dependence of these properties on the initial dielectric function of the sample and the DOS of the sample. Furthermore, we have seen that the evolution of optical quantities is non-trivially connected to laser input parameters.

All together, we have shown, that the model for the optical parameters produces results that are in agreement with the experimental data by Obergfell et al. [5]. We have noted, that improvements in the optical modeling can yet be made for instance by fitting the dielectric function more precisely, but the total approach can be successfully applied to copper. We have hence confiremed, that the assumption of immediate electron thermalization to Fermi distributions has been reasonable for picosecond timescales.

7 Conclusion

In this thesis, the evolution of electron occupation densities and temperatures in copper after ultrafast laser-excitation was investigated, based on the two-temperature model and a two-band rate equation model. The model includes the two outer bands of copper, such the $3d$- and the $4sp$-band. The absorption of laser light and the distribution of energy on short timescales in noble metals were discussed in this context. Several equilibrium and non-equilibrium stages were found. With the assumption of immediate thermalization to a Fermi distribution with a shared temperature in the two bands, a second stage of band equilibrium between the chemical potentials and occupation densities was found. The final stage of equilibrium was described as the equilibrium between electrons and phonons.

Furthermore, a model to describe optical properties of the laser-excited sample based on the two temperatures of the TTM and the occupation densities of both electronic bands was applied and investigated for copper. Finally, reflectivity and transmissivity of the sample were calculated. They were calculated for extracted parameters of copper and conditions experimentally tested conditions. The variation of the initial parameters of the dielectric function based on a generalized Drude-Lorentz model showed a strong influence on the simulation results. The simulated data was compared to the experimental data by Obergfell et al. [5]. The underlying modulation of the Drude and Lorentz parameters based on internal parameters of the copper sample, proved to work as a general approach for simplified modeling of optical properties in copper.

The model based on calculations introduced for gold and designed for NIR and visible excitation was applicable to the investigation of copper as a different noble metal. This confirmed the assumption of immediate themalization of electrons to Fermi distributions for the investigation on picosecond timescales.

8 Outlook

After testing the model on a first set of experimental data and conditions, it can be expanded, improved and understood more carefully, taking into account the following points.

8.1 Variation of parameters

The final results in Chapter 6 are presented for different underlying DOS and fit parameters of the dielectric function. Yet, the influence of individual parameters on the final results was not yet properly investigated. An investigation of the strength of influence of several parameters could not only lead to improved results, but also to a better understanding of the model and perhaps the underlying physics.

As the electron-electron relaxation times are not well established yet, a comparison of the final results, for different relaxation times might yield new insights or perhaps even better results. As seen in Fig. 4.3, the impact of the relaxation time on electron behavior, is indeed quite strong.

Regarding the *sp*-densities, we saw in Fig. 4.3, that due to numerical errors, the calculations may yield incorrect results for conditions with low energies. This was the case for simulations with the application of the pump pulse parameters from Table 4.1(a). Those errors can be minimized by comparing the model to other experimental data in higher energy ranges.

Furthermore, due to the important role of the initial Drude-Lorentz fit, a variation in the amount of Lorentz oscillators might improve the model or lead to the creation of a new description.

To model the optical properties with the dielectric function, the Lorentz terms and therefore the Lorentz parameters $\omega_{0,j}$, Γ_j and f_j are essential for the final results. Yet, we have only discussed them collectively in order to obtain reflectivity and transmissivity maps. The investigation of the actual time dependence of the individual parameters might highly increase the understanding of the matter. The time dependence in this context, is more accurately a temperature and electron occupation dependence. Furthermore by holding the other parameters constant, the importance of each parameter for the final development of reflectivity and transmissivity can be determined.

Similar investigations can be made for the time-development of other quantities like n_{sp}. The influence of the electron-phonon coupling on the electron density relaxation, can for example be investigated, by simulating the development without electron-phonon coupling ($g_{ei} = 0$) for comparison.

8.2 Quantification of Correlation

The correlation between the experimental and the simulated data was compared on the basis of few superficial attributes, of the resulting R- and T-maps. The quantification of the similarity with mathematical methods, could on the long term yield more accurate understanding of the limits of the model.

At a first step, the data could be investigated at a fixed time after laser-excitation and compared and illustrated with one dimensional-methods. This would easily give a more accurate quantification for the location of extrema in the spectrum of probe frequencies.

8.3 Further Improvements of Inaccuracies in the Model

We fit only the real part of the dielectric function in Section 5.2 for reasons of simplicity. As the results show to be strongly influenced by the fitted initial parameters of the dielectric function, an improvement of the fit accuracy might be beneficial. Such an improvement can be made by fitting to the more sensitive imaginary part of the dielectric function as well. Methods for finding the optimized total fit for both functions can be used, in order to increase the accuracy of the fitted parameters and therefore improve the final results.

In Eq. (5.14c), the damping frequency of the Lorentz oscillators is modeled, to change with changing electron-electron scattering. However, possible changes in electron-phonon scattering are neglected, due to their minor effect for the situation with low excitation energies. These changes can not be implemented as the electron-phonon scattering of free electrons, as for the electron-electron scattering. This is, because the initial damping already represents the electron-phonon scattering. Based on that, one approach for modeling the damping change is, to introduce the initial damping frequency as,

$$\Gamma_j^{in} = \gamma_j 300\,\mathrm{K} \tag{8.1}$$

similar to the description of ν_{ei}, with a constant parameter γ_j. The electron-phonon damping for higher lattice temperatures would then result as $\Gamma_j^{ei} = \gamma_j T_i$, resulting in a new damping modification of,

$$\Gamma_j(t) = \gamma_j T_i(t) + \nu_{ee}(t), \tag{8.2}$$

instead of Eq. (5.14c).

Finally, the numerical calculations are based on certain assumptions. For example, that $c_{T_e}^x$ and p_μ^x have non-zero values in Eq. (3.12) and Eq. (3.13). For very low excitation energies and photon frequencies, this might actually not be given or the values might be lower, than allowed by the representation in the computer. For these conditions, the model reaches its limit. However, more advanced numerical methods and different analytical implementations of the equation system may be used, in order to make the model applicable on such extreme situations. Still, other assumptions are made in the description itself, such that the model is limited by other means as well in its range of applicability.

Bibliography

[1] A. Ancona, F. Röser, K. Rademaker, J. Limpert, S. Nolte, and A. Tünnermann. High speed laser drilling of metals using a high repetition rate, high average power ultrafast fiber cpa system. *Optics Express*, **16**(12) 8958–8968 (2008).

[2] M. Bauer, A. Marienfeld, and M. Aeschlimann. Hot electron lifetimes in metals probed by time-resolved two-photon photoemission. *Progress in Surface Science*, **90**(3) 319 – 376 (2015).

[3] D. Kraus, J. Vorberger, A. Pak, N. J. Hartley, L. B. Fletcher, S. Frydrych, E. Galtier, E. J. Gamboa, D. O. Gericke, S. H. Glenzer, E. Granados, M. J. MacDonald, A. J. MacKinnon, E. E. McBride, I. Nam, P. Neumayer, M. Roth, A. M. Saunders, A. K. Schuster, P. Sun, T. van Driel, T. Döppner, and R. W. Falcone. Formation of diamonds in laser-compressed hydrocarbons at planetary interior conditions. *Nature Astronomy*, **1**(9) 606–611 (2017).

[4] A. L. Kritcher, D. C. Swift, T. Döppner, B. Bachmann, L. X. Benedict, G. W. Collins, J.n L. DuBois, F. Elsner, G. Fontaine, J. A. Gaffney, S. Hamel, A. Lazicki, W. R. Johnson, N. Kostinski, D. Kraus, M. J. MacDonald, B. Maddox, M. E. Martin, P. Neumayer, A. Nikroo, J. Nilsen, B. A. Remington, D. Saumon, P. A. Sterne, W. Sweet, A. A. Correa, H. D. Whitley, R. W. Falcone, and S. H. Glenzer. A measurement of the equation of state of carbon envelopes of white dwarfs. *Nature*, **584**(7819) 51–54 (2020).

[5] M. Obergfell and J. Demsar. Tracking the time evolution of the electron distribution function in copper by femtosecond broadband optical spectroscopy. *Physical Review Letters*, **124** 037401 (2020).

[6] H. E. Elsayed-Ali, T. B. Norris, M. A. Pessot, and G. A. Mourou. Time-resolved observation of electron-phonon relaxation in copper. *Physical Review Letters*, **58** 1212–1215 (1987).

[7] X. Shen, Y. P. Timalsina, T. Lu, and M. Yamaguchi. Experimental study of electron-phonon coupling and electron internal thermalization in epitaxially grown ultrathin copper films. *Physical Review B*, **91** 045129 (2015).

[8] P. D. Ndione, S. T. Weber, B. Rethfeld, and D. O. Gericke. Density response to short-pulse excitation in gold. *Contributions to Plasma Physics*, **59**(4-5) e201800186 (2019).

[9] P. D. Ndione, D. O. Gericke, and B. Rethfeld. Optical properties of gold after intense short-pulse excitations. *Frontiers in Physics*, **10** (2022).

[10] C. Guo and A. J. Taylor. Ultrafast electronic disorder in heat-induced structural deformations and phase transitions in metals. *Physical Review B*, **62** 5382–5386 (2000).

[11] S. E. Kirkwood, Y. Y. Tsui, R. Fedosejevs, A. V. Brantov, and V. Yu. Bychenkov. Experimental and theoretical study of absorption of femtosecond laser pulses in interaction with solid copper targets. *Physical Review B*, **79** 144120 (2009).

[12] S. D. Brorson, J. G. Fujimoto, and E. P. Ippen. Femtosecond electronic heat-transport dynamics in thin gold films. *Physical Review Letters*, **59**(17) 1962 (1987).

[13] A. Nakamura, T. Shimojima, M. Nakano, Y. Iwasa, and K. Ishizaka. Electron and lattice dynamics of transition metal thin films observed by ultrafast electron diffraction and transient optical measurements. *Structural Dynamics*, **3**(6) 064501 (2016).

[14] S. I. Anisimov, B. L. Kapeliovich, and T. L. Perel'man. Electron emission from metal surfaces exposed to ultrashort laser pulses. *Soviet Physics JETP*, **39** 375–377 (1974).

[15] E.Y. Tsymbal. Optical properties of solids. `https://unlcms.unl.edu/cas/physics/tsymbal/teaching/SSP-927/Section%2013_Optical_Properties_of_Solids.pdf`. Access: 01.07.2022.

[16] E. Silaeva, L. Saddier, and J. P. Colombier. Drude-lorentz model for optical properties of photoexcited transition metals under electron-phonon nonequilibrium. *Applied Sciences*, **11**(21) (2021).

[17] M. Born and E. Wolf. *Principles of optics - Electromagnetic theory of propagation, interference and diffraction of light.* Cambridge University Press, 7. Auflage, 1999.

[18] C. Seibel. tbd. Master, Technische Universität Kaiserslautern, 2020.

[19] Nils Brouwer and Baerbel Rethfeld. Transient electron excitation and nonthermal electron-phonon coupling in dielectrics irradiated by ultrashort laser pulses. *Physical Review B*, **95** 245139 (2017).

[20] B. Y. Mueller, T. Roth, M. Cinchetti, M. Aeschlimann, and B. Rethfeld. Driving force of ultrafast magnetization dynamics. *New Journal of Physics*, **13**(12) 123010 (2011).

[21] J. C. Fuggle, E. Källne, L. M. Watson, and D. J. Fabian. Electronic structure of aluminum and aluminum-noble-metal alloys studied by soft-x-ray and x-ray photoelectron spectroscopies. *Physical Review B*, **16** 750–761 (1977).

[22] H. P. Loock, L. M. Beaty, and B. Simard. Reassessment of the first ionization potentials of copper, silver, and gold. *Physical Review A*, **59** 873–875 (1999).

[23] Fhi-aims code. URL `https://fhi-aims.org`.

[24] E. Bévillon, J. P. Colombier, V. Recoules, and R. Stoian. Free-electron properties of metals under ultrafast laser-induced electron-phonon nonequilibrium: A first-principles study. *Physical Review B*, **89** 115117 (2014).

[25] S. T. Weber and B. Rethfeld. Laser-excitation of electrons and nonequilibrium energy transfer to phonons in copper. *Applied Surface Science*, **417** 64–68 (2017).

[26] Z. Lin, L. V. Zhigilei, and V. Celli. Electron-phonon coupling and electron heat capacity of metals under conditions of strong electron-phonon nonequilibrium. *Physical Review B*, **77**(7) 075133 (2008).

[27] N. Medvedev and I. Milov. Electron-phonon coupling in metals at high electronic temperatures. *Physical Review B*, **102**(6) 064302 (2020).

[28] P. Ji and Y. Zhang. Ab initio determination of effective electron–phonon coupling factor in copper. *Physics Letters A*, **380**(17) 1551–1555 (2016).

[29] B. Y. Mueller and B. Rethfeld. Relaxation dynamics in laser-excited metals under nonequilibrium conditions. *Physical Review B*, **87**(3) 035139 (2013).

[30] B. Y. Mueller and B. Rethfeld. Nonequilibrium electron–phonon coupling after ultrashort laser excitation of gold. *Applied Surface Science*, **302** 24–28 (2014).

[31] N J Simon, E S Drexler, and R P Reed. Properties of copper and copper alloys at cryogenic temperatures. final report (1992).

[32] J A Cahill and A D Kirshenbaum. The density of liquid copper from its melting point (1356 k.) to 2500 k. and an estimate of its critical constants. *Journal of Physical Chemistry (U.S.)* ().

[33] P. B. Johnson and R. W. Christy. Optical constants of the noble metals. *Physical Review B*, **6** 4370–4379 (1972).

[34] K. Stahrenberg, Th. Herrmann, K. Wilmers, N. Esser, W. Richter, and M. J. G. Lee. Optical properties of copper and silver in the energy range 2.5–9.0 ev. *Physical Review B*, **64** 115111 (2001).

[35] H. S. Sehmi, W. Langbein, and E. A. Muljarov. Optimizing the drude-lorentz model for material permittivity: Method, program, and examples for gold, silver, and copper. *Physical Review B*, **95** 115444 (2017).

[36] O. Peña-Rodríguez. Modelling the dielectric function of au-ag alloys. *Journal of Alloys and Compounds*, **694** 857–863 (2017).

[37] T. Williams, C. Kelley, and many others. Gnuplot 5.4. `http://www.gnuplot.info/`, January 2022.

[38] C. Fourment, F. Deneuville, D. Descamps, F. Dorchies, S. Petit, and O. Peyrusse. Experimental determination of temperature-dependent electron-electron collision frequency in isochorically heated warm dense gold. *Physical Review B*, **89** 161110–1–161110–5 (2014).

[39] N. W. Ashcroft and N. D. Mermin. *Solid State Physics*. Oldenbourg, München Wien, 3. Auflage, 2007.

[40] R.E. Stephens and I.H. Malitson. Index of refraction of magnesium oxide. *Journal of Research of the National Bureau of Standards*, **49**(4) 249–252 (1952).

Erklärung

Verwendete Software

Alle Plots in dieser Arbeit wurden mit Graphics Layout Engine erstellt. Die numerischen Rechnungen wurden unter Verwendung der Programmbibliotheken GSL und Boost in C++ durchgeführt. Dieses Dokument wurde mit LaTeX erstellt.

Ich versichere, dass ich die vorliegende Arbeit selbstständig verfasst und keine anderen als die angegebenen Quellen und Hilfsmittel verwendet sowie Zitate kenntlich gemacht habe.

Kaiserslautern, den

Marius Wenk